Chapter 4

The Influence of Weaving Patterns on the Effective Mechanical Response of Reinforced Composites - A Study Through Homogenization

Chapter details

Chapter DOI:

https://doi.org/10.4322/978-65-86503-83-8.c04

Chapter suggested citation / reference style:

da Rocha, Jonas T., et al. (2022). "The Influence of Weaving Patterns on the Effective Mechanical Response of Reinforced Composites - A Study Through Homogenization". *In* Jorge, Ariosto B., et al. (Eds.) *Fundamental Concepts and Models for the Direct Problem*, Vol. II, UnB, Brasilia, DF, Brazil, pp. 76–119. Book series in Discrete Models, Inverse Methods, & Uncertainty Modeling in Structural Integrity.

P.S.: DOI may be included at the end of citation, for completeness.

Book details

Book: Fundamental Concepts and Models for the Direct Problem

Edited by: Jorge, Ariosto B., Anflor, Carla T. M., Gomes, Guilherme F., & Carneiro, Sergio H. S.

Volume II of Book Series in:

Discrete Models, Inverse Methods, & Uncertainty Modeling in Structural Integrity

Published by: UnB City: Brasilia, DF, Brazil Year: 2022

DOI: https://doi.org/10.4322/978-65-86503-83-8

The Influence of Weaving Patterns on the Effective Mechanical Response of Reinforced Composites - A Study Through Homogenization

Jonas Tieppo da Rocha[1], Tales Vargas de Lisbôa[2] and Rogério José Marczak[3*]

[1]Mechanical Engineering Department, UFRGS, Porto Alegre, Brazil.
E-mail: jonas.tieppo@ufrgs.br
[2]Mechanics and Composite Materials Department, Leibniz Institute of Polymer Research, Dresden, Germany, E-mail: tales-lisboa@ipfdd.de
[3*]Mechanical Engineering Department, UFRGS, Porto Alegre, Brazil.
E-mail: rato@mecanica.ufrgs.br
[*]Corresponding author

Abstract

A study on the influence of the waving patterns on the mechanical response of textile composites is presented. Three typical weaving patterns of industrial interest are explored, as well as a case of cross-ply laminate composite. Homogenization techniques were employed, with the RVE being subjected to well-known displacement and periodic boundary conditions. Owing to the reduced thickness to span ratio usually found in engineering applications of textile composites, we proposed a different set of boundary conditions to disregard repetition along the transverse direction. All boundary conditions were verified to satisfy Hill-Mandel energy equivalence. The engineering constants estimated for the four composites and three sets of boundary conditions are obtained and compared through anisotropy indices and the Frobenius norm of the stiffness. The reduced constitutive tensor, used in thin plate and shell problems, is also derived from their homogenized 3D counterparts and discussed. The strain fields are also investigated for one textile, and the engineering constants were used in a test case to illustrate the weave pattern influence in an actual component.

1 Introduction

Fiber-reinforced composites can be roughly divided into two categories when the size of the fibers and how they are arranged/distributed in the matrix phase are taken into account: (a) particulate, when the fibers are short enough to disregard its geometry and spatial orientation, and (b) fiber-reinforced, when the reinforcement phase is continuous or at least long enough so that its orientation has considerable influence on the overall mechanical behavior of the component. Other sub-categories can be drawn, however, our interest lies in fiber-reinforced composites or, more specifically, composites built by interlacing bundles of fiber in a repetitive pattern commonly known as textile composites.

In the traditional composite manufacturing processes, fiber-reinforced composites are manufactured by laminating several layers of unidirectional fiber laminae embedded in a pre-impregnated matrix material. The effective properties of the composite can be controlled by changing fiber orientation in a layer, stacking sequence, fiber and matrix material properties, and constituents volume fraction combination. This method of manufacturing is labor-intensive and does not allow transverse (through-the-thickness) fiber reinforcement, resulting in poor interlaminar strength [ming Huang, 2000, Sankar and Marrey, 1997].

As an alternative, textile processes such as weaving, braiding, and knitting can produce larger volumes of material at faster rates. In these techniques, bundles of fiber are interlaced following a specific pattern (fig. 1), then impregnated with a suitable matrix material and cured in a mold to provide the final form. The 2D woven and braided laminae thus manufactured offer increased through-the-thickness and impact resistance properties as a consequence of the bundle interlacing [Mazumda, 2002]. Because the interlocking is in general different in the thickness direction, this kind of structure is sometimes called 2.5D textile structures [Sankar and Marrey, 1997]. These processes allow the manufacturing of complex-shaped components as integral units, reducing or eliminating the use of joints, glues, and fasteners. These advances in manufacturing, however, demand the development of analytical approaches to predict the performance of the components made by these processes.

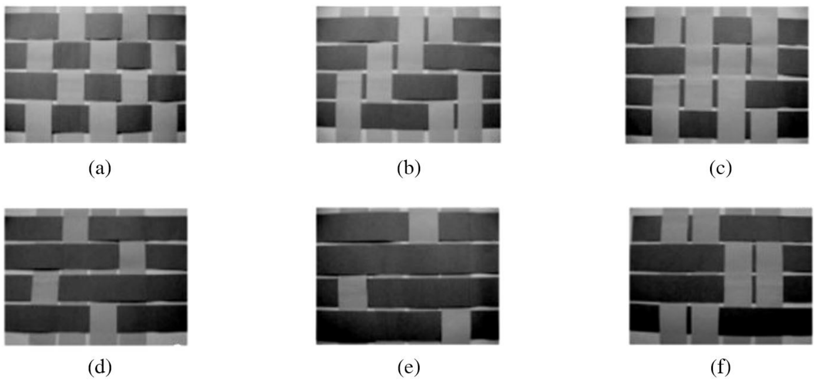

Figure 1: Schematics of woven composites without matrix pockets: (a) plain weave; (b) 2×2 twill weave; (c) 4-harness satin weave; (d) 5-harness satin weave; (e) 8-harness satin weave; (f) basket weave (Dixit and Mali [2013]).

Textile composites which in most ways behave like laminates fall into the category of laminar textiles, while those in which triaxial stresses exist and incorporate weaving along the transverse direction as well. The present study aims at the first category. We re-examine homogenization procedures used to compute the effective (macroscopic) properties of woven composites, as well as the nature of the boundary data which may be assigned to an RVE. The overall effective moduli for linearly elastic RVEs of three common textile composites are thoroughly studied, under a set of uniform boundary traction, linear boundary displacements, and periodic conditions. Special attention is given to mixed boundary conditions, culminating in a proposal of a new set of boundary conditions to be used with RVE analysis, aiming its usage with thin plate/shell finite element (FEA) or boundary element (BEA) analysis.

Stiffness constitutive relations for 3D elastic as well as their 2D thin-plate counterparts for three types of textile composites are analyzed and compared to available results. Average mechanical constants are retrieved for both cases and discussed. The results show that the differences in the macroscopic behavior caused by inherent mechanisms associated with particular weaving patterns are captured using homogenization, which is very difficult to be distinguished when average field theories are used.

Throughout the text, we assume familiarization with Elasticity Theory, index notation, as well as knowledge of the essentials of homogenization, RVE analysis, and average field theory.

2 Modeling Composites Reinforced by Weave Fibers

The modeling of composites reinforced by woven fabrics can be divided into two methodologies: analytical or numerical. The analytical approaches are usually based on physical measurements of the constituents and possibly ruled by some type of averaging calculation. The importance of analytical solutions lies in their ability to represent the mechanical behavior of the composite and give insights to the project, like bending-extension coupling magnitudes, overall stiffness, and approximated failure loads. However, they are limited if the designer wants to explore more complex constructions of fiber and matrix. Furthermore, most analytical forms are based on the Classical Laminate Theory (CLT). Assumptions of such approach neglect the shear in the thickness direction (out of plane), which makes the analysis incapable of predicting some effects like delamination. Computational methodologies are more powerful, can be extended to non-linear phases, but is generally computer-intensive.

Due to the complex microstructure of woven composites, computational homogenization is commonly used for the estimation of their elastic constants. In the present case, numerical modeling of a RVE is usual because of its ability to capture the effects of complicated textile architectures. If these effects are not precisely represented, the mechanical properties of the textile composite, which serves as input data for analyzing the response of the structural components made from this composite, become compromised.

Ideally, a two-step homogenization approach to predict the effective properties should be used. The first homogenization step (micro-homogenization) deals with determining the effective properties of tows (bundles) from fiber and matrix properties. The second homogenization step (macro-homogenization), is actually used to retrieve the effective properties. In the present work, only the second step will be used, considering that industrial tows used in textile composites are well tested and documented. This approach is by far the most used by researchers in this field. The other important aspect is the type of boundary condition which should be used on textiles, also discussed here.

Therefore, it is clear that the homogenization analysis of thin textile composites has differences if compared to the analysis of a general 3D anisotropic solid, and this is reflected in many important contributions in the literature. Barbero et al. [2006] employed periodic boundary conditions on the homogenization of a plain-weave, comparing the results with experiments and the CLT approach. The results showed an excellent agreement with the experiments, overcoming the CLT procedure, especially on the effective shear modulus determination. Rao et al. [2008] also applied periodic boundary conditions on the study of the effect of the textile architecture on its mechanical properties. The author also studied the influence of debonding between fibers and the surrounding matrix, by applying a unit-cell along with a cohesive zone model. The approach showed good agreement with experimental results, especially when debonding is considered. Jacques et al. [2014] studied a general application of periodic boundary conditions for textiles and proposed an approach to circumvent the requirement of a periodic mesh by applying constraints on reference nodes along the boundaries of the RVE. Ullah et al. [2019] implemented a complete computational framework for predicting the elastic behavior of 2D and 3D textiles composites. The implementation employed three boundaries conditions types: static uniform boundary conditions, periodic boundary conditions, and uniform traction boundary conditions. Results showed a difference smaller than 5% between the tested boundary conditions and experimental data. Espadas-Escalante et al. [2017] reached a distinct result: the effective elastic results differ for textile composites. In this study, the uniform traction conditions were not adequate to predict E_{11} and E_{22} elastic moduli. The author proposed a set of mixed boundary conditions which were the combination of an out-of-plane traction condition (not necessarily null) and periodic boundary conditions for the plane directions. Results for mixed boundary conditions performed better for E_{11} modulus.

Regardless of the approach employed to predict effective material properties, analytical or numerical, it must be capable of embodying the particular strain field in the repeating cell for each pattern, even when they have the same fiber volume fraction. With average field theories, this will, in general, deliver the same result.

2.1 Analytical approach

Let a point in a three-dimensional medium characterized by its stress-strain state in Voigt notation (Jones [2018]), i.e.:

$$\boldsymbol{\sigma} = \begin{pmatrix} \sigma_{11} \\ \sigma_{22} \\ \sigma_{33} \\ \sigma_{13} \\ \sigma_{23} \\ \sigma_{12} \end{pmatrix} , \qquad \boldsymbol{\varepsilon} = \begin{pmatrix} \varepsilon_{11} \\ \varepsilon_{22} \\ \varepsilon_{33} \\ \varepsilon_{13} \\ \varepsilon_{23} \\ \varepsilon_{12} \end{pmatrix} . \tag{1}$$

The most general constitutive relation between $\boldsymbol{\sigma}$ and ε, with the thermodynamic and tensor symmetry constraints already considered, is the generalized Hooke's law:

$$\boldsymbol{\sigma} = \mathrm{C}\,\boldsymbol{\varepsilon} \ , \tag{2}$$

where C contains up to 21 different constitutive constants. Laminated composites generally have a high aspect ratio, allowing to model most structural elements under the simplifications of plate or shell models. Although very limited for industrial applications, plate models reduce the equilibrium equations to the point of obtaining simplified analytical solutions containing essential information regarding the deformation kinematics, like in-plane and bending stress and strain. For the sake of simplicity, herein we will consider only plate models under the linear elastic regime.

The plate's mid-surface is generally considered as a reference plane, which lies on the (x_1, x_2) plane so that the thickness h is measured through the x_3-axis, $x_3 = [-h/2, +h/2]$. Among the several laminated plate models proposed, most of the analytical solutions are based on Classical Laminate Theory (CLT), which employs the classic thin plate kinematics. Therefore, it is advisable to recall the main Kirchhoff's hypothesis for plates:

1. Transverse normal fibers initially straight and perpendicular to the reference surface remain so after the deformation;

2. Transverse normal fibers inextensible.

As a consequence, transverse shear strains (ε_{13} and ε_{23}) and the transverse normal strain (ε_{33}) are neglected, reducing the number of strains to three. The number of non-null stress follows Hooke's law, except that the transverse normal stress is *ad hoc* assumed zero, characterizing the well-known inconsistency of thin plate theory. The generalized Hooke's law (eq. (2)) now reduces to:

$$\begin{pmatrix} \sigma_{11} \\ \sigma_{22} \\ \sigma_{12} \end{pmatrix} = \begin{bmatrix} C_{11} & C_{12} & C_{13} \\ C_{12} & C_{22} & C_{23} \\ C_{13} & C_{23} & C_{33} \end{bmatrix} \begin{pmatrix} \varepsilon_{11} \\ \varepsilon_{22} \\ \varepsilon_{12} \end{pmatrix} , \tag{3}$$

or, for short:

$$\boldsymbol{\sigma} = \bar{\bar{\mathbf{C}}}\boldsymbol{\varepsilon} , \tag{4}$$

where $\bar{\bar{\mathbf{C}}}$ corresponds to the reduced constitutive matrix (Jones [2018]).

The plate resultant stresses (stresses by unit length) are evaluated by integrating the local stresses throughout the thickness, resulting in the in-plane (extensional or membrane) and out-of-plane (bending) stresses:

$$\mathbf{N} = \begin{pmatrix} N_{11} \\ N_{22} \\ N_{12} \end{pmatrix} = \int_h \begin{pmatrix} \sigma_{11} \\ \sigma_{22} \\ \sigma_{12} \end{pmatrix} \mathrm{d}x_3 , \tag{5}$$

$$\mathbf{M} = \begin{pmatrix} M_{11} \\ M_{22} \\ M_{12} \end{pmatrix} = \int_h \begin{pmatrix} \sigma_{11} \\ \sigma_{22} \\ \sigma_{12} \end{pmatrix} x_3 \, \mathrm{d}x_3 . \tag{6}$$

The following additional assumptions are used to include the case of laminated plates (CLT):

3. The laminas are perfectly bonded;

4. Each lamina is linear-elastic and orthotropic;

5. The strain field is continuous through the plate thickness.

Now recall that the strain field $\boldsymbol{\sigma}$ of eq. (3) can also be split into its extensional (membrane) and bending parts:

$$\boldsymbol{\varepsilon} = \boldsymbol{\varepsilon}^m + x_3\,\boldsymbol{\kappa}\;, \tag{7}$$

where $\boldsymbol{\varepsilon}^m$ accounts for extension/shear deformations while $\boldsymbol{\kappa}$ accounts for curvature changes of the plate. After inserting eq. (7) into eq. (3), the latter can be integrated in the thickness direction – eqs. (5) and (6) (Reddy [2003]), adding the contribution of each lamina. The basic resultant stress-strain of the CLT is then obtained:

$$\begin{pmatrix} \mathbf{N} \\ \mathbf{M} \end{pmatrix} = \begin{bmatrix} \mathbf{A} & \mathbf{B} \\ \mathbf{B} & \mathbf{D} \end{bmatrix} \begin{pmatrix} \boldsymbol{\varepsilon}^m \\ \boldsymbol{\kappa} \end{pmatrix}\;, \tag{8}$$

where $\mathbf{A}$, $\mathbf{B}$, and $\mathbf{D}$ are the extensional, bending-extension coupling, and bending *stiffness* matrices, respectively. The inverse of these coefficients is denoted as $\mathbf{a}^*, \mathbf{b}^*, \mathbf{d}^*$, respectively, whenever *compliance* coefficients are needed. Besides using stress-resultants, eq. (8) must be further distinguished from eq. (3) because it already incorporates Kirchhoff's plate model kinematics, so it will be called ABD-matrix.

2.1.1 Ishikawa and Chou model

One of the first approaches to evaluate analytically the stiffness of woven composites that have been published is the well-known series model presented by Ishikawa [1981], who provided closed-form solutions for the macroscopic coupling coefficients of the $\mathbf{B}$ submatrix. The model is based on Kirchhoff's plate theory as well, and therefore it is an interesting method to be compared to other solutions. Here, the effects of temperature are not considered, although, in the original formulation Ishikawa [1981], the expressions are complete. A simple comparison example is the expressions for the ABD-matrix in eq. (8), in terms of engineering constants for a two-lamina cross-ply plate simulating a plain-weave composite were derived as:

$$A_{11} = A_{22} = h\,\frac{(E_{11}+E_{22})}{2} = h\,\frac{(E_{LL}+E_{TT})}{2\,(1-\upsilon_{LT}\upsilon_{TT})}\;, \tag{9a}$$

$$A_{12} = h\,E_{12} = h\,\frac{\upsilon_{LT}E_{TT}}{(1-\upsilon_{LT}\upsilon_{TT})}\;, \tag{9b}$$

$$A_{66} = h\,E_{66} = h\,G_{LT}\;, \tag{9c}$$

$$B_{11} = -B_{22} = \frac{(E_{11}-E_{22})\,h^2}{8} = \frac{(E_{LL}-E_{TT})\,h^2}{8\,(1-\upsilon_{LT}\upsilon_{TT})}\;, \tag{9d}$$

$$D_{11} = D_{22} = \frac{(E_{11}+E_{22})\,h^3}{24} = \frac{(E_{LL}+E_{TT})\,h^3}{24\,(1-\upsilon_{LT}\upsilon_{TT})}\;, \tag{9e}$$

$$D_{12} = \frac{E_{66}h^3}{12} = \frac{\upsilon_{LT}E_{LL}h^3}{12\,(1-\upsilon_{LT}\upsilon_{TT})}\;, \tag{9f}$$

$$D_{66} = \frac{E_{66}h^3}{12} = \frac{G_{LT}h^3}{12}\;, \tag{9g}$$

where L and T are the main material directions of the laminae.

The basic idea of the series model is to neglect the two-dimensional character of the plate and assume a repetitive occurrence of an alternating two-layer beam cell with length $2a$. If the cell is repeated n times, average stress or strain can be retrieved by integration.

Let the model be subjected to a uniform traction $N = (N_{11}\ \ 0\ \ 0)^T$. The average curvature can be evaluated as Ishikawa [1981]:

$$\bar{\kappa}_{11} = \frac{1}{na} \int_0^{na} \kappa_{11} \mathrm{d}x \ . \tag{10}$$

This leads to simple expressions for the average values of the compliance coefficients $\mathbf{a}^*$ and $\mathbf{b}^*$. Considering yet that in a cross-ply laminate, if stacking sequence is inverted the coupling terms change sign, the average curvature is:

$$\bar{\kappa}_{11} = \left(1 - \frac{2}{n}\right) b^*_{11} N_1 \ , \tag{11}$$

implying that the corrected compliance b^w_{11} coefficient for a two-layer weaving composite is:

$$b^{*w}_{11} = \left(1 - \frac{2}{n}\right) b^*_{11} \ . \tag{12}$$

Similar considerations are made for other coefficients, leading additionally to:

$$\begin{aligned} a^{*w}_{11} &= a^*{}_{11} \ , \\ d^{*w}_{11} &= d^*{}_{11} \ . \end{aligned} \tag{13}$$

The inversion of the abd-matrix, given by eqs. (12) and (13), generates a corrected ABD-matrix which gives the lower bound of the stiffness:

$$\begin{aligned} D^w_{ij} &= \left\{ d^*_{ij} - \left(1 - \frac{2}{n}\right)^2 b^*_{ik} a^*_{kl} \left(b^*_{lj}\right)^{-1} \right\}^{-1} \ , \\ B^w_{ij} &= -\left(1 - \frac{2}{n}\right) \left(a^*_{ik}\right)^{-1} b^*_{kl} D^w_{lij} \ , \\ A^w_{ij} &= \left(a^*_{ij}\right)^{-1} + \left(1 - \frac{2}{n}\right)^2 \left(a^*_{ik}\right)^{-1} b^*_{kl} D^w_{km} b^*_{mn} \left(a^*_{nj}\right)^{-1} \ . \end{aligned} \tag{14}$$

In order to obtain the corresponding upper bound, the average in-plane stresses can be evaluated considering uniform membrane and bending strains along the length of the model. For instance (Ishikawa [1981]):

$$\begin{aligned} \bar{N}_{11} &= \frac{1}{na} \int_0^n a N_1 \, \mathrm{d}x \\ &= A_{11} \varepsilon^m_{11} + A_{12} \varepsilon^m_{22} + \left(1 - \frac{2}{n}\right) B_{11} \kappa_{11} \ , \end{aligned} \tag{15}$$

and the corrected plate stiffness coefficients follow directly. They represent the stiffness upper bounds:

$$
\begin{aligned}
A_{ij}^{w} &= A_{ij} \ , \\
B_{ij}^{w} &= \left(1 - \frac{2}{n}\right) B_{ij} \ , \\
D_{ij}^{w} &= D_{ij} \ ,
\end{aligned} \tag{16}
$$

with the coefficients of the right-hand side calculated from eq. (9). Figure 2 shows the upper and lower bounds for b_{11}^* and A_{11} as functions of the repetition frequency. It must be noted that, for a plain-weave, $n = 2$ and the coupling b_{11}^* vanishes.

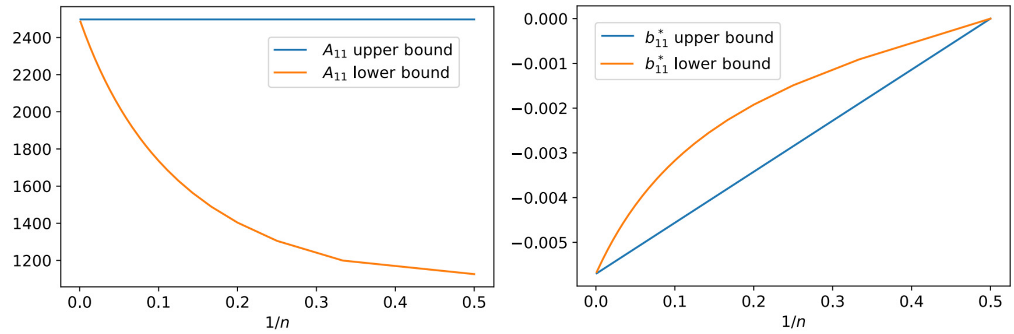

(a) (b)

Figure 2: Upper and lower bounds of for (a) A_{11} and (b) b_{11}^* as in Ishikawa [1981].

2.2 Numerical approach

2.2.1 RVE

The *Representative Volume Element* (RVE) provides a useful tool to relate the microstructure and the overall (or effective) properties of a heterogeneous solid (Nemat-Nasser and Hori [1996], Hill [1963]). RVE-based approaches to classical multi-scale solid mechanics with both macro and micro-scales described in terms of conventional kinematics are very well understood and lie on solid theoretical grounds set in the works of Hill [1972] and Mandel [1998]. Therefore, they constitute a particularly well-suited methodology to be applied in the present context, since the main interest lies in the analysis of the macroscopic linear elastic constitutive relation for a class of composites.

An RVE must structurally represent the whole solid regarding an average value of the property P, that is, it must contain an adequate volume of material (or size D) such as to represent the effective mechanical properties of the material in a statistically homogeneous way, regardless the size of the material features (λ). As an analogy, fig. 3 illustrates a study of the color perception (property P) of an image for varying number of pixels (of size λ) in the RVE of length D sampled from the image. The length D is conventionally equal to the repeating unit cell (RUC) dimension. Nemat-Nasser and Hori [1996] claim that the RVE must include the features which have a first-order impact on the homogenized properties. Therefore, in metallurgical research, for instance, a couple of microns could be considered a micro-scale, and hundreds of microns could be defined as a macro-scale or continuum scale. On the other hand, in composite mechanics, the

RVE should have at least some millimeters to contain enough reinforcements that could capture properly macroscopic properties. In the general case, it is not possible to establish a RUC, hence D can be any real number. By regulating the size of the RVE, is expected that the property P will asymptotically reach a stable value for a computationally acceptable number of RUCs. The solid is therefore homogenized, hence one can apply the right techniques to retrieve its overall properties.

Since the present study is focused on composites whose reinforcement phase of the material is weaved, forming a fabric-like pattern, one could take advantage of the periodic structure, and represent the RVE by a number of RUCs. In this case, the required number of RUCs is relatively low, as it will be shown in the following sections. It is important to note that a homogenization analysis based on RVE is different than what is postulated by the average field theory. The average field theory is based on the physics and experimental definition of the overall properties of heterogeneous solids. In a RVE size analysis, on the other hand, establish relations between the micro-scale and the macro-scale using some sort of multi-scale perturbation technique. The properties will reach asymptotically to a macro value, as illustrated in fig. 3. At this point, the number of heterogeneities categorizes statistically macro-properties, and a procedure can be derived to determine, for example, the engineering constants of the media.

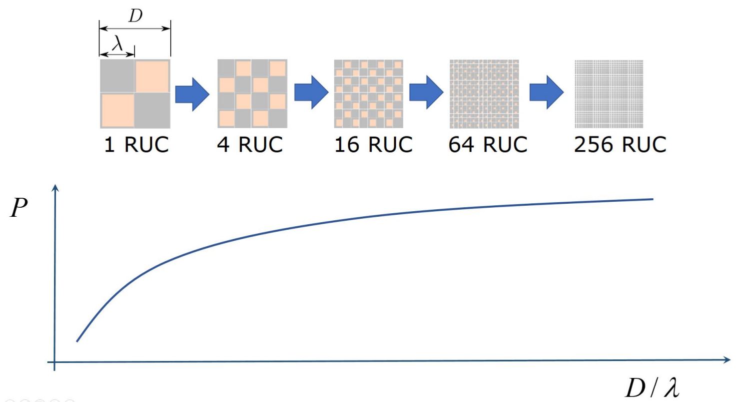

Figure 3: Exemplification of a RVE size and convergence of an overall property P.

2.2.2 Boundary conditions

The boundary conditions imposed on the RVE play a key role in the analysis. They must obey minimum requirements in order to ensure energy equivalence between the average and the local stress and strain states (Nemat-Nasser and Hori [1996]). In most cases, the typical boundary conditions used in RVE analysis fall into three categories: static uniform boundary conditions (SUBC), kinematic uniform boundary conditions (KUBC), and periodic boundary conditions (PBC) (Hazanov and Amieur [1995], Espadas-Escalante et al. [2017]). In this work, an additional type of boundary condition will be proposed, derived from a combination of the others, herein referred to as mixed boundary conditions (MBC).

The aforementioned energy equivalence, also known as the Hill-Mandel Principle of Macro-homogeneity (or just Hill's energy criteria, for short), must be satisfied by all boundary conditions and will be explored in the context of static problems under linear regime (Hill [1965], Mandel [1998], de Souza Neto and Feijóo [2008]). Denoting the volumetric average as $\langle\cdot\rangle_V$, the macro-stress and macro-strain defined over a material sample are:

$$\begin{aligned}\langle\sigma_{ij}\rangle_V &= \frac{1}{|V|}\int_V \sigma_{ij}\mathrm{d}V \ , \\ \langle\varepsilon_{ij}\rangle_V &= \frac{1}{|V|}\int_V \varepsilon_{ij}\mathrm{d}V \ .\end{aligned} \tag{17}$$

Evidently, σ_{ij} and ε_{ij} are the stresses and strains at a microscopic level, so that Hooke's law must refer to a point $\mathbf{x} \in \mathbf{V}$:

$$\sigma_{ij}(\mathbf{x}) = C_{ijkl}(\mathbf{x})\varepsilon_{kl}(\mathbf{x}) \ . \tag{18}$$

At the macroscopic level, the elastic tensor represents an average constitutive relation in V, and therefore:

$$\langle\sigma_{ij}\rangle_V = \bar{C}_{ijkl}\langle\varepsilon_{kl}\rangle_V \ , \tag{19}$$

where the dependence on the size V is in evidence.

Hill's energy condition requires that the average strain energy density $\langle U\rangle$ is equivalent to both states. By using eqs. (18) and (19), one has, in the absence of stress rates:

$$\langle U\rangle_V = \frac{1}{2}\langle\varepsilon_{ij}C_{ijkl}\varepsilon_{kl}\rangle = \frac{1}{2}\langle\langle\varepsilon_{ij}\rangle_V\bar{C}_{ijkl}\langle\varepsilon_{kl}\rangle_V\rangle \ , \tag{20}$$

or

$$\langle\sigma_{ij}\varepsilon_{ij}\rangle_V = \langle\sigma_{ij}\rangle_V\langle\varepsilon_{ij}\rangle_V \ . \tag{21}$$

Before proceeding into the details of each type of boundary condition, it is important to prove the relationship between $\langle\varepsilon_{kl}\rangle_V$ and the boundary conditions of the SUBC type, i.e.:

$$u_i|_{\partial V} = \varepsilon^A_{ij}x_j \ , \tag{22}$$

where ε^A_{ij} denotes a prescribed constant strain state, and x corresponds to a position vector. From the average strain definition (eq. (17)), we have:

$$\langle\varepsilon_{ij}\rangle_V = \frac{1}{2V}\int_V\left(\frac{\partial u_i}{\partial x_j} + \frac{\partial u_j}{\partial x_i}\right)\mathrm{d}V \ . \tag{23}$$

For generality, let's assume that volume V is composed of two subregions of volume V_1 and V_2 connected by an interface volume $V_1 \cap V_2$, so that $V = V_1 + V_2 + V_1 \cap V_2$ as shown in fig. 4.

Under this volume partition, eq. (23) is rewritten:

$$\langle\varepsilon_{ij}\rangle_V = \frac{1}{2V}\left[\int_V\left(\frac{\partial u_i}{\partial x_j} + \frac{\partial u_j}{\partial x_i}\right)\mathrm{d}V + \int_{V_1\cap V_2}\left(\frac{\partial u_i}{\partial x_j} + \frac{\partial u_j}{\partial x_i}\right)\mathrm{d}V\right] \ , \tag{24}$$

which can be converted into a boundary-only equation using the divergence theorem:

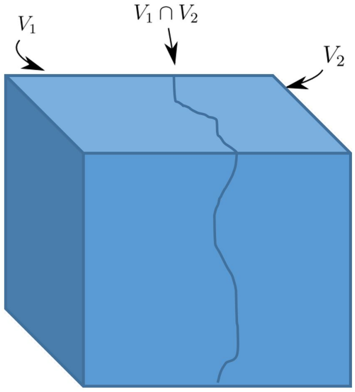

Figure 4: Division of a volume V into three parts.

$$\langle \varepsilon_{ij} \rangle_V = \frac{1}{2V} \left[\int_{\partial V} (u_i n_j + u_j n_i)\, \mathrm{d}A + \int_{\partial V_1 \cap \partial V_2} (u_i n_j + u_j n_i)\, \mathrm{d}A \right] . \tag{25}$$

Now the boundary condition (eq. (22)) can be imposed, resulting in:

$$\begin{aligned} \langle \varepsilon_{ij} \rangle_V &= \frac{1}{2V} \left[\int_{\partial V} \left(\varepsilon^A_{ij} x_j n_j + \varepsilon^A_{ij} x_i n_i \right) \mathrm{d}A + \int_{\partial V_1 \cap \partial V_2} (u_i n_j + u_j n_i)\, \mathrm{d}A \right] , \\ &= \frac{1}{2|V|} \left[\int_V \left(\frac{\partial}{\partial x_j} \left(\varepsilon^A_{ij} x_j \right) + \frac{\partial}{\partial x_i} \left(\varepsilon^A_{ji} x_i \right) \right) \mathrm{d}V + \int_{\partial V_1 \cap \partial V_2} (u_i n_j + u_j n_i)\, \mathrm{d}A \right] , \end{aligned} \tag{26}$$

which, after manipulation, simplifies to:

$$\langle \varepsilon_{ij} \rangle_V = \varepsilon^A_{ij} + \frac{1}{2V} \int_{\partial V_1 \cap \partial V_2} (u_i n_j + u_j n_i)\, \mathrm{d}A . \tag{27}$$

The term $u_i n_j + u_j n_i$ in eq. (27) represents the jump in the displacement field along with the interface between V_1 and V_2. Whenever the volumes are perfectly bonded, the boundary integral terms vanishes, resulting in the equivalence known as *Average Strain Theorem*, written as:

$$\langle \varepsilon_{ij} \rangle_V = \varepsilon^A_{ij} . \tag{28}$$

2.2.3 Static uniform boundary conditions

Once eq. (28) is demonstrated and proved, it is possible to detail the different boundary condition types. As aforementioned, the Static Uniform Boundary Conditions (SUBC) is established if the displacements on the boundary are described as in eq. (22). Other authors, such as Espadas-Escalante et al. [2017] and Shen and Brinson [2006], alternatively named it Uniform Displacement Boundary Condition, as proposed by Hazanov and Amieur [1995]. Essentially, the SUBC is a kinematically admissible displacement field that creates a homogeneous strain field. For example, if a pure-extension condition is imposed on a cube, such as shown in fig. 5, one writes:

$$\boldsymbol{\varepsilon}^A = \begin{bmatrix} \varepsilon_{11}^A & 0 & 0 \\ 0 & 0 & 0 \\ 0 & 0 & 0 \end{bmatrix} .$$

If the global coordinate system is placed at the cube center, it is trivial to write:

$$u|_{\mathbf{x}_i=(a_1,0,0)^T} = -\, u|_{\mathbf{x}_i=(-a_1,0,0)^T} = \varepsilon_{11}^A a_1 ,$$

where a_1 is the half-length of the cube.

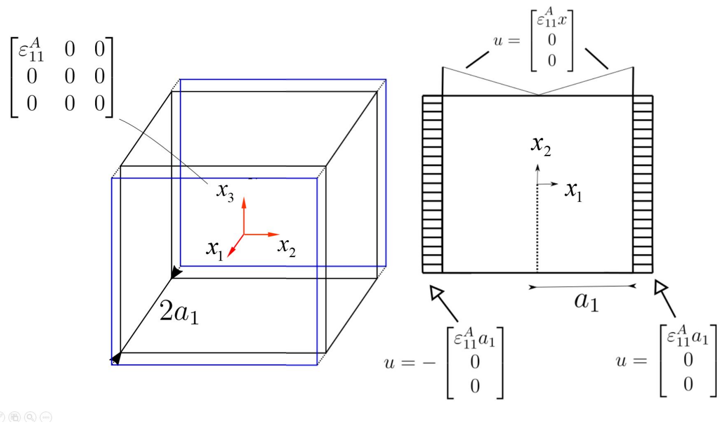

Figure 5: Boundary conditions scheme for the ε_A state.

Now it is necessary to show that Hill's energy condition is satisfied for the boundary condition $u_i|_{\partial V} = \varepsilon_{ij}^A x_j$. The work done by the surface traction t_i on the surface ∂V of the solid is written:

$$\begin{aligned} \int_{\partial V} u_i t_i \mathrm{d}A &= \int_{\partial V} u_i \sigma_{ij} n_j \; \mathrm{d}A , \\ &= \int_V \frac{\partial}{\partial x_j}\Big(u_i \sigma_{ij}\Big) \; \mathrm{d}V , \\ &= \int_V (\frac{\partial}{\partial x_j} u_i) \sigma_{ij} \; \mathrm{d}V , \\ &= \int_V \varepsilon_{ij} \sigma_{ij} \; \mathrm{d}V . \end{aligned} \tag{29}$$

Alternatively, one can write:

$$\begin{aligned} \int_{\partial V} u_i t_i \mathrm{d}A &= \int_{\partial V} \varepsilon_{ij}^A x_j \sigma_{ij} n_j \; \mathrm{d}A , \\ &= \int_V \frac{\partial}{\partial x_j}\Big(\varepsilon_{ij}^A x_j\Big) \sigma_{ij} \; \mathrm{d}V , \\ &= \int_V \varepsilon_{ij}^A \sigma_{ij} \; \mathrm{d}V . \end{aligned} \tag{30}$$

One can recall the Average Strain Theorem (eq. (28)) and observe that the resultants of eqs. (29) and eqs. (30) prove the energy equivalence, since:

$$\langle \varepsilon_{ij} \rangle_V \sigma_{ij} \equiv \varepsilon_{ij}^A \sigma_{ij} \; . \tag{31}$$

2.2.4 Periodic boundary conditions

Luciano and Sacco [1998] introduced the evaluation concept of the overall properties of a periodic media subjected to either a mean strain or mean stress field. In a periodic prism $2a_1 \times 2a_2 \times 2a_3$ (see fig. 6), the displacement field on its boundary can be written as:

$$u_i(a_1, x_2, x_3) - u_i(-a_1, x_2, x_3) = 2\varepsilon_{i1} a_1, \forall x_2 \in [-a_2, a_2], \forall x_3 \in [-a_3, a_3] \; , \tag{32a}$$
$$u_i(x_1, a_2, x_3) - u_i(x_1, -a_2, x_3) = 2\varepsilon_{i2} a_2, \forall x_1 \in [-a_1, a_1], \forall x_3 \in [-a_3, a_3] \; , \tag{32b}$$
$$u_i(x_1, x_2, a_3) - u_i(x_1, x_2, -a_3) = 2\varepsilon_{i3} a_3, \forall x_1 \in [-a_1, a_1], \forall x_2 \in [-a_2, a_2] \; . \tag{32c}$$

Equation (32) is known as Periodic Boundary Conditions (PBC). Further details of the derivation of eqs. (32) are omitted in this text. They can be found, however, in Luciano and Sacco [1998]. The micro-strains and micro-stresses within the periodic media are represented by the equations:

$$\varepsilon_{ij}(x_1, x_2, x_3) = \varepsilon_{ij}^0 + \varepsilon_{ij}^p(x_1, x_2, x_3) \; , \tag{33}$$

$$\sigma_{ij}(x_1, x_2, x_3) = \sigma_{ij}^0 + \sigma_{ij}^p(x_1, x_2, x_3) \; , \tag{34}$$

where ε_{ij}^0 and σ_{ij}^0 represent the mean strains and mean stresses, respectively. ε_{ij}^p and σ_{ij}^p are the V-periodic strain and stresses. Those entities are defined by the following expressions:

$$\varepsilon_{ij}^0 = \frac{1}{V} \int_V \varepsilon_{ij}(x_1, x_2, x_3) dV = \langle \varepsilon_{ij} \rangle_V \; , \tag{35a}$$
$$\sigma_{ij}^0 = \frac{1}{V} \int_V \sigma_{ij}(x_1, x_2, x_3) dV = \langle \sigma_{ij} \rangle_V \; , \tag{35b}$$
$$0 = \frac{1}{V} \int_V \varepsilon_{ij}^p(x_1, x_2, x_3) dV \; , \tag{35c}$$
$$0 = \frac{1}{V} \int_V \sigma_{ij}^p(x_1, x_2, x_3) dV \; . \tag{35d}$$

Equations (32) establish a relationship between displacements over opposite faces. Therefore, the displacements are not directly imposed, differently from what eq.(22) proposes. Aiming at their computational implementation, eq.(32a) can be rewritten as:

$$u_i(a_1, x_2, x_3) - u_i(-a_1, x_2, x_3) = \begin{bmatrix} \varepsilon_{11} & \varepsilon_{12} & \varepsilon_{13} \\ \varepsilon_{21} & \varepsilon_{22} & \varepsilon_{23} \\ \varepsilon_{31} & \varepsilon_{32} & \varepsilon_{33} \end{bmatrix} \begin{bmatrix} a_1 \\ 0 \\ 0 \end{bmatrix} \; . \tag{36}$$

The same procedure is applied to eqs. (32b) and (32c) as well. Equation (36) indicates that opposite faces are subjected to the restrictions defined at the center position of each one. They produce, however, ambiguities at vertices and along edges, as they can have over-defined boundary conditions, as clarified by Barbero [2007].

Considering a periodic body like the one depicted in fig. 6, symmetric edges respective to the center of the body must be tied. In order to exemplify future computational implementation, edges parallel to x_3 must respect the following condition:

$$u_i(a_1, a_2, x_3) - u_i(-a_1, -a_2, x_3) = \begin{bmatrix} \varepsilon_{11} & \varepsilon_{12} & \varepsilon_{13} \\ \varepsilon_{21} & \varepsilon_{22} & \varepsilon_{23} \\ \varepsilon_{31} & \varepsilon_{32} & \varepsilon_{33} \end{bmatrix} \begin{bmatrix} a_1 \\ a_2 \\ 0 \end{bmatrix} . \tag{37}$$

And vertices such those lying on $x_i = (a_1, a_2, a_3)$ and $x_i = (-a_1, -a_2, -a_3)$ must be tied by:

$$u_i(a_1, a_2, a_3) - u_i(-a_1, -a_2, a_3) = \begin{bmatrix} \varepsilon_{11} & \varepsilon_{12} & \varepsilon_{13} \\ \varepsilon_{21} & \varepsilon_{22} & \varepsilon_{23} \\ \varepsilon_{31} & \varepsilon_{32} & \varepsilon_{33} \end{bmatrix} \begin{bmatrix} a_1 \\ a_2 \\ a_3 \end{bmatrix} . \tag{38}$$

Analogous equations can be defined for others vertices and edges.

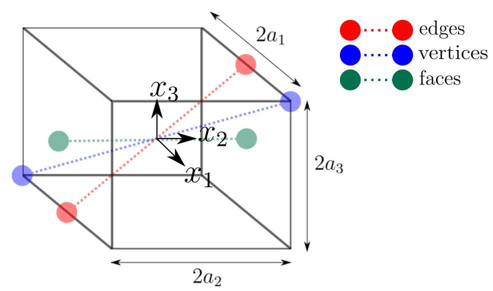

Figure 6: Definition of geometric entities for the periodic boundary conditions scheme.

The satisfaction of Hill's energy condition for this type of boundary condition is not easily found in the literature. For sake of completeness, a short proof can be derived. Hazanov and Amieur [1995], among others, showed that the following equivalence holds:

$$\int_{\partial V} \Big(t_i - \langle \sigma_{ij} \rangle n_j \Big) \cdot \Big(u_i - \langle \varepsilon_{ij} \rangle x_j \Big) \, \mathrm{d}A = 0 \quad \Leftrightarrow \quad \langle \sigma_{ij} \varepsilon_{ij} \rangle_V - \langle \sigma_{ij} \rangle_V \langle \varepsilon_{ij} \rangle_V = 0 \, , \tag{39}$$

which can be transformed in a volume integral as:

$$\frac{1}{V} \int_V \Big(\sigma_{ij} - \langle \sigma_{ij} \rangle_V \Big) \cdot \Big(\varepsilon_{ij} - \langle \varepsilon_{ij} \rangle_V \Big) \, \mathrm{d}V = \langle \sigma_{ij} \varepsilon_{ij} \rangle_V - \langle \sigma_{ij} \rangle_V \langle \varepsilon_{ij} \rangle_V = 0 \, . \tag{40}$$

Inserting eqs. (33) and (34) in eq. (40) and expanding the resultant, one obtains:

$$\begin{split} \frac{1}{V} \int_V \Big(\sigma^0_{ij} \varepsilon^0_{ij} - \sigma^0_{ij} \langle \varepsilon_{ij} \rangle_V - \langle \sigma_{ij} \rangle_V \varepsilon^0_{ij} + \sigma^0_{ij} \varepsilon^p_{ij} + \sigma^p_{ij} \varepsilon^0_{ij} + \sigma^p_{ij} \varepsilon^p_{ij} + \\ - \sigma^p_{ij} \langle \varepsilon_{ij} \rangle_V - \langle \sigma_{ij} \rangle_V \varepsilon^p_{ij} + \langle \sigma_{ij} \rangle_V \langle \varepsilon_{ij} \rangle_V \Big) \, dV = \langle \sigma_{ij} \varepsilon_{ij} \rangle_V - \langle \sigma_{ij} \rangle_V \langle \varepsilon_{ij} \rangle_V = 0 \, , \end{split} \tag{41}$$

and, by canceling out the equivalent terms in eq. (41), one can write:

$$\frac{1}{V}\int_V \sigma^p_{ij}\varepsilon^p_{ij}\,\mathrm{d}V = 0 \; . \tag{42}$$

Another way to see eq. (42) comes up by interpreting it as a simple circular convolution between two periodic signals σ and ε with period V, i.e. $\int_V \sigma\varepsilon\,\mathrm{d}V$ which in this case, results in a function with the same period. Because the signals are symmetric, the convolution must be zero.

2.2.5 Mixed boundary conditions

One of the first applications of Mixed Boundary Conditions (MBC) in the context of the RVE homogenization problem was presented by Hazanov and Amieur [1995], accounting for both traction (p_i) and displacement (u_i) boundary values as follows:

$$\Big(p_i - \langle\sigma_{ij}\rangle_V n_j\Big)\Big(u_i - \langle\varepsilon_{ij}\rangle_V x_j\Big) = 0 \; , \quad \text{on} \quad \partial V \; , \tag{43}$$

therefore, combining sets of KUBC and SUBC. It is important to highlight that this type of boundary condition is limited to elastic materials that show orthotropic symmetry, at most. Any less symmetric material, i.e., monoclinic or triclinic symmetries, would generate coupling stresses that would not respect eq. (43). A great advantage of this approach is to reproduce effectively the boundary conditions from experimental tests, as in Shen and Brinson [2006], which imposed KUBC in faces perpendicular to the loading and SUBC on faces parallel to the loading.

Recently, in a general homogenization scheme proposed by Glüge [2013], the RVE boundary is divided into *n* parts, each one subjected to an average strain $\langle\varepsilon_{ij}\rangle_V$:

$$\langle\varepsilon_{ij}\rangle_V \int_{\partial V_n} x_j n_i dA = \int_{\partial V_n} u_j n_i \,\mathrm{d}A \; . \tag{44}$$

The above equation leads to important remarks:

1. If $n \to \infty$, then $u|_{\partial V} = \varepsilon^A_{ij}x_j$ as in SUBC.

   Proof: The integral drops in (44) and it follows that:

$$\begin{aligned} \langle\varepsilon_{ij}\rangle_V x_j n_i dA &= u_j n_i dA, \textit{ in } \partial V \; , \\ u|_{\partial V} &= \langle\varepsilon_{ij}\rangle_V x_j \; , \\ u|_{\partial V} &= \varepsilon^A_{ij} x_j \; . \end{aligned} \tag{45}$$

2. If $n \to \infty$, when the faces are mirrored such that $n_i dA^+ = -n_i dA^-$, eq.(44) corresponds to a PBC.

   Proof: Equation (44) is divided into $n_i dA^+$ and $n_i dA^-$, with position vectors $x^+_j = -x^-_j$, the superscripts meaning opposite sides of an RVE as follows:

$$\begin{aligned} \langle\varepsilon_{ij}\rangle_V x^+_j n_i dA^+ + \langle\varepsilon_{ij}\rangle_V x^-_j n_i dA^- &= u^+_i n_j dA^+ + u^-_i n_j dA^- \; , \\ 2\langle\varepsilon_{ij}\rangle_V x^+_j &= u^+_i - u^-_i \; . \end{aligned} \tag{46}$$

   This is equivalent to eq. (32).

3. If $n = 1$, $\partial V_n \to \partial V$, and eq.(44) represents KUBC. Equation (44) then becomes:

$$\langle \varepsilon_{ij} \rangle_V = \frac{1}{V} \int_{\partial V} u_i n_j \, \mathrm{d}A \ , \tag{47}$$

which can be shown to correspond to a homogeneous stress field.

In a study focused on textiles made by Espadas-Escalante et al. [2017], the concept of MBC as a combination of PBC and KUBC is proposed. In the plane directions, the composite is treated as periodic, while in the out-of-plane direction uniform traction is imposed. This allows applying a traction-free condition along the out-of-plane direction, which replicates the plane-stress condition expected in thin structures such as textiles. Emphasis is given to the fact that *”homogenization is highly dependent of boundary conditions’ choosing for one layer of textile composite”*. The most important results can be numbered as:

- Differences between SUBC and KUBC on E_{11} homogenization can vary as much as 200%;
- MBC approach asymptotically PBC as the number of layers is increased in a laminate;
- The out-of-plane E_{33} seems to be less sensitive than E_{11} to boundary condition type (differences of 10%);
- The results showed that SUBC and PBC performed better in comparison to experimental results for in-plane mechanical properties.

3 A New Set of Boundary Conditions

The study of Espadas-Escalante et al. [2017] motivated the implementation of a different set of MBC. Since PBC and SUBC deliver better results when compared to experimental data, the basic idea is to mix PBC for the in-plane degrees of freedom and SUBC for the out-of-plane degrees of freedom, trying to extract the best of both sets of boundary conditions. This proposal will be referenced as MBC* along with this chapter.

Considering again a prism $2a_1 \times 2a_2 \times 2a_3$ with a centered coordinate system, the degrees of freedom in the 1-2 directions are specified as proposed by Luciano and Sacco [1998], while for direction 3, SUBC is used. Each face is identified by its relative position: West, East, North, South, Upper, and Lower, as in fig.7. Naturally, for the degrees of freedom in the plane 1-2 the stress and strain fields admit the distribution given by eqs. (33) and (34), repeated below for convenience. No *a priori* assumptions are made for the strain and stress fields along the out-of-plane axis (x_3).

$$\varepsilon_{ij}(x_1, x_2, x_3) = \langle \varepsilon_{ij} \rangle_V + \varepsilon^p_{ij}(x_1, x_2, x_3) \ , \quad \text{for } i = 1, 2 \ , \tag{48a}$$

$$\sigma_{ij}(x_1, x_2, x_3) = \langle \sigma_{ij} \rangle_V + \sigma^p_{ij}(x_1, x_2, x_3) \ , \quad \text{for } i = 1, 2 \ , \tag{48b}$$

$$\int_V \varepsilon^p_{ij}(x_1, x_2, x_3) \, \mathrm{d}V = 0 \ , \tag{48c}$$

$$\int_V \sigma^p_{ij}(x_1, x_2, x_3) \, \mathrm{d}V = 0 \ . \tag{48d}$$

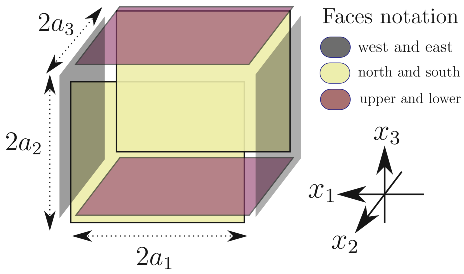

Figure 7: Face notation for the proposed set of boundary conditions.

Therefore, one has on the West and East faces:

$$\begin{cases} u_1(a_1, x_2, x_3) - u_1(-a_1, x_2, x_3) = 2\varepsilon^A_{11} a_1 \ , & \forall\ x_1 \in (-a_1, a_1) \ , \\ u_2(a_1, x_2, x_3) - u_2(-a_1, x_2, x_3) = 2\varepsilon^A_{21} a_1 \ , & \forall\ x_2 \in [-a_2, a_2] \ , \\ u_3(a1, x_2, x_3) = -u_3(-a_1, x_2, x_3) = \varepsilon^A_{3j} x_j \ , & \forall\ x_3 \in [-a_3, a_3] \ , \end{cases} \tag{49}$$

and on the North and South faces:

$$\begin{cases} u_1(x_1, a_2, x_3) - u_1(x_1, -a_2, x_3) = 2\varepsilon^A_{11} a_2 \ , & \forall\ x_1 \in [-a_1, a_1] \ , \\ u_2(x_1, a_2, x_3) - u_2(x_1, -a_2, x_3) = 2\varepsilon^A_{21} a_2 \ , & \forall\ x_2 \in (-a_2, a_2) \ , \\ u_3(x_1, a_2, x_3) = -u_3(x_1, -a_2, x_3) = \varepsilon^A_{3j} x_j \ , & \forall\ x_3 \in [-a_3, a_3] \ , \end{cases} \tag{50}$$

while on the Upper and Lower faces:

$$\begin{cases} u_1(x_1, x_2, a_3) - u_1(x_1, x_2, -a_3) = 2\varepsilon^A_{11} a_2 \ , & \forall\ x_1 \in [-a_1, a_1] \ , \\ u_2(x_1, x_2, a_3) - u_2(x_1, x_2, -a_3) = 2\varepsilon^A_{21} a_2 \ , & \forall\ x_2 \in [-a_2, a_2] \ , \\ u_3(x_1, x_2, a_3) = -u_3(x_1, x_2, -a_3) = \varepsilon^A_{3j} x_j \ , & \forall\ x_3 \in (-a_3, a_3) \ . \end{cases} \tag{51}$$

By analyzing the proposed boundary conditions in terms of the Average Strain Theorem, the volume average is carried out to the boundary by the divergence theorem as follows:

$$\begin{aligned} \langle \varepsilon_{ij} \rangle_V &= \frac{1}{|V|} \int_V \varepsilon_{ij} \ \mathrm{d}V \ , \\ &= \frac{1}{2|V|} \int_V \left(\frac{\partial u_i}{\partial x_j} + \frac{\partial u_j}{\partial x_i} \right) \mathrm{d}V \ , \\ &= \frac{1}{2|V|} \int_{\partial V} \Big(u_i n_j + u_j n_i \Big) \ \mathrm{d}A \ . \end{aligned} \tag{52}$$

The boundary can be divided into six parts, according to the colored faces of fig. 7:

$$\partial V = \partial V^e + \partial V^w + \partial V^n + \partial V^s + \partial V^u + \partial V^l \tag{53}$$

hence:

$$\begin{aligned}\langle \varepsilon_{ij} \rangle_V =& \frac{1}{2|V|} \left\{ \int_{\partial V^e} \left(u_i^e n_j^e + u_j^e n_i^e \right) \mathrm{d}A + \int_{\partial V^w} \left(u_i^w n_j^w + u_j^w n_i^w \right) \mathrm{d}A + \ldots \right. \\ & \left. \int_{\partial V^u} \left(u_i^u n_j^u + u_j^u n_i^u \right) dA + \int_{\partial V^l} \left(u_i^l n_j^l + u_j^l n_i^l \right) \mathrm{d}A \right\} , \\ =& \frac{1}{2|V|} \left\{ \Psi^{w/e} + \Psi^{n/s} + \Psi^{u/l} \right\} .\end{aligned} \tag{54}$$

On the West and East faces, noting that $n^e = -n^w$:

$$\Psi^{w/e} = \int_{\partial w/e} \left\{ (u_i^e - u_i^w) n_j^e + (u_j^e - u_j^w) n_i^e \right\} \mathrm{d}A . \tag{55}$$

Noting also that $u_i^e = u_i(a_1, x_2, x_3)$ and $u_i^w = u_i(-a_1, x_2, x_3)$, by using the boundary conditions of eq. (49):

$$\Psi^{w/e} = 2 \int_{\partial w/e} \begin{bmatrix} 2\varepsilon_{11} a_1 \\ 2\varepsilon_{21} a_1 \\ 2\varepsilon_{3i} x_i \end{bmatrix} \begin{bmatrix} n_1^e & n_2^e & n_3^e \end{bmatrix} \mathrm{d}A , \tag{56}$$

and observing that $n^e = [1 \;\; 0 \;\; 0]$:

$$\Psi^{w/e} = 4 \int_{\partial w/e} \begin{bmatrix} \varepsilon_{11} a_1 & 0 & 0 \\ \varepsilon_{21} a_1 & 0 & 0 \\ \varepsilon_{3i} x_i & 0 & 0 \end{bmatrix} \mathrm{d}A . \tag{57}$$

Since the third line requires a particular approach, one writes it separately. The first step is to split the expression into three integrals, written by:

$$\begin{aligned}\int_{\partial w/e} \varepsilon_{3i} x_i \mathrm{d}A &= \int_{\partial w/e} \left(\varepsilon_{31} a_1 + \varepsilon_{32} x_2 + \varepsilon_{33} x_3 \right) \mathrm{d}x_2 \, \mathrm{d}x_3 , \\ &= \varepsilon_{31} a_1 (4 a_2 a_3) + \varepsilon_{32} \left. \frac{x_2^2}{2} \right|_{-a_2}^{a_2} \cdot 2a_3 + \varepsilon_{33} \left. \frac{x_3^2}{2} \right|_{-a_3}^{a_3} \cdot 2a_2 , \\ &= \varepsilon_{31} a_1 (4 a_2 a_3) .\end{aligned} \tag{58}$$

One notices that the last two terms of the second line vanish because $\left. \frac{x_2^2}{2} \right|_{-a_2}^{a_2} = \left. \frac{x_3^2}{2} \right|_{-a_3}^{a_3} = 0$. The eq. (57) can be rewritten as follows:

$$\Psi^{w/e} = \begin{bmatrix} \varepsilon_{11} & 0 & 0 \\ \varepsilon_{21} & 0 & 0 \\ \varepsilon_{31} & 0 & 0 \end{bmatrix} 2|V| , \tag{59}$$

where $|V| = 8 a_1 a_2 a_3$. Taking similar steps fo$\Psi^{n/s}$ and $\Psi^{u/l}$, we arrive at:

$$\Psi^{n/s} = \begin{bmatrix} 0 & \varepsilon_{12} & 0 \\ 0 & \varepsilon_{22} & 0 \\ 0 & \varepsilon_{33} & 0 \end{bmatrix} 2|V| , \tag{60}$$

$$\Psi^{u/l} = \begin{bmatrix} 0 & 0 & \varepsilon_{13} \\ 0 & 0 & \varepsilon_{23} \\ 0 & 0 & \varepsilon_{33} \end{bmatrix} 2|V| \; . \tag{61}$$

Now eqs. (59), (60), and (61) can be inserted into the expression for $\langle \varepsilon_{ij} \rangle_V$ (eq. (54)) and resulting in:

$$\langle \varepsilon_{ij} \rangle_V = \begin{bmatrix} \varepsilon_{11} & \varepsilon_{12} & \varepsilon_{13} \\ \varepsilon_{21} & \varepsilon_{22} & \varepsilon_{23} \\ \varepsilon_{31} & \varepsilon_{32} & \varepsilon_{33} \end{bmatrix} = \varepsilon^A_{ij} \; , \tag{62}$$

which proves that the Average Strain Theorem holds for the eqs. (49)- (51).

In order to verify if this set of boundary conditions complies the Hill's energy condition, one follows the approach introduced by Hazanov and Amieur [1995]. It is worth noting that eq. (39) is automatically satisfied if $u_i = \langle \varepsilon_{ij} \rangle_V x_j$ on ∂V and this is readily verified for u_3. Nonetheless, for the remaining degrees-of-freedom, further investigation must be performed. Firstly, one rewrites eq. (40) for u_1 and u_2, and using the divergence theorem, obtaining (Hazanov and Amieur [1995]):

$$\frac{1}{V}\int_V \Big(\sigma_{1j} - \langle \sigma_{1j} \rangle_V\Big) \cdot \Big((\varepsilon_{1j} - \langle \varepsilon_{1j} \rangle_V\Big) dV = 0 \; , \tag{63a}$$

$$\frac{1}{V}\int_V \Big(\sigma_{2j} - \langle \sigma_{2j} \rangle_V\Big) \cdot \Big((\varepsilon_{2j} - \langle \varepsilon_{2j} \rangle_V\Big) dV = 0 \; , \tag{63b}$$

$$\int_{\partial V} \Big(t_3 - \langle \sigma_{3j} \rangle_V \, n_j\Big) \cdot \Big((u_3 - \langle \varepsilon_{3j} \rangle_V \, x_j\Big) dA = 0 \; . \tag{63c}$$

As already mentioned, considering the third equation in eqs. (49)-(51) on any of the boundary surfaces, $u_3 = \langle \varepsilon_{3j} \rangle \, x_j$ and eq. (63c) vanishes automatically, in view of eq. (62). For u_1 and u_2, the same steps applied to prove Hill's criteria for periodic boundary conditions can be used, along with the stress and strain fields of eq.(48), leading to a similar result of eq. (42) as follows:

$$\frac{1}{V}\int_V \sigma^p_{ij}\varepsilon^p_{ij} \, \mathrm{d}V = 0 \; , \quad i = 1, 2 \; .$$

4 Evaluation of Effective Elastic Properties

The basic procedure to evaluate the effective elastic constants is well known (Zohdi [2002]). Essentially, eq. (19), repeated below for convenience, must be solved for RVE subjects to any of the boundary conditions discussed in the previous sections:

$$\langle \sigma_{ij} \rangle_V = \bar{C}_{ijkl} \langle \varepsilon_{kl} \rangle_V \; . \tag{64}$$

Now if the local stress field $\boldsymbol{\sigma}$ can be numerically calculated through either a FE or a BE analysis, so is $\langle \boldsymbol{\sigma} \rangle_V$, and eq. (64) provides six equations. One way to overcome the insufficient number of equations is by solving the RVE problem for other types of boundary conditions. This will provide the necessary equations to recover all entries of $\bar{\mathbf{C}}$

in the macroscopic constitutive relation of eqs. (64). Given the dimensions of $\bar{\mathrm{C}}$, applying six independent strain states will suffice (see fig. 8):

$$\begin{aligned}
\varepsilon^1 &= \begin{bmatrix} \varepsilon_{xx} & 0 & 0 \\ 0 & 0 & 0 \\ 0 & 0 & 0 \end{bmatrix}, \quad \varepsilon^2 = \begin{bmatrix} 0 & 0 & 0 \\ 0 & \varepsilon_{yy} & 0 \\ 0 & 0 & 0 \end{bmatrix}, \quad \varepsilon^3 = \begin{bmatrix} 0 & 0 & 0 \\ 0 & 0 & 0 \\ 0 & 0 & \varepsilon_{zz} \end{bmatrix}, \\
\varepsilon^4 &= \begin{bmatrix} 0 & \varepsilon_{xy} & 0 \\ \varepsilon_{xy} & 0 & 0 \\ 0 & 0 & 0 \end{bmatrix}, \quad \varepsilon^5 = \begin{bmatrix} 0 & 0 & \varepsilon_{xz} \\ 0 & 0 & 0 \\ \varepsilon_{xz} & 0 & 0 \end{bmatrix}, \quad \varepsilon^6 = \begin{bmatrix} 0 & 0 & 0 \\ 0 & 0 & \varepsilon_{yz} \\ 0 & \varepsilon_{yz} & 0 \end{bmatrix}.
\end{aligned} \tag{65}$$

The final system of linear equations can be derived as:

$$\begin{bmatrix} \langle\sigma^1\rangle_{6\times1} \\ \langle\sigma^2\rangle_{6\times1} \\ \langle\sigma^3\rangle_{6\times1} \\ \langle\sigma^4\rangle_{6\times1} \\ \langle\sigma^5\rangle_{6\times1} \\ \langle\sigma^6\rangle_{6\times1} \end{bmatrix}_V = \begin{bmatrix} [C]_{6\times6} & [0]_{6\times6} & \cdots & \cdots & \cdots & [0]_{6\times6} \\ [0]_{6\times6} & [C]_{6\times6} & [0]_{6\times6} & \cdots & \cdots & [0]_{6\times6} \\ \vdots & [0]_{6\times6} & [C]_{6\times6} & [0]_{6\times6} & \cdots & [0]_{6\times6} \\ \vdots & \vdots & [0]_{6\times6} & [C]_{6\times6} & [0]_{6\times6} & [0]_{6\times6} \\ \vdots & \vdots & \vdots & [0]_{6\times6} & [C]_{6\times6} & [0]_{6\times6} \\ [0]_{6\times6} & \cdots & \cdots & \cdots & [0]_{6\times6} & [C]_{6\times6} \end{bmatrix} \begin{bmatrix} \langle\varepsilon^1\rangle \\ \langle\varepsilon^2\rangle \\ \langle\varepsilon^3\rangle \\ \langle\varepsilon^4\rangle \\ \langle\varepsilon^5\rangle \\ \langle\varepsilon^6\rangle \end{bmatrix}_V, \tag{66}$$

where $\langle\sigma^k\rangle$ and $\langle\varepsilon^k\rangle$, $k = 1..6$ are the average stress and strain states in Voigt notation. Equation (66) can be optimized for computational implementation. Starting with the vectorization of each $[C]$ sub-matrix:

$$[C]_{36\times1} = [M]^{-1}_{36\times36} \, [\langle\sigma\rangle_V]_{36\times1} \,, \tag{67}$$

with $\mathbf{M} = [\mathbf{M}^1_{ab} \ldots \mathbf{M}^k_{ab}]^T_{k=1..6}$, where k is one of the strain cases in eq.(65), and $\mathbf{M}^k_{ab}$ is the concatenated matrix (6 lines $\times$ 36 columns):

$$\mathbf{M}^k_{ab} = \begin{cases} \left[\langle\varepsilon^k\rangle_1 \ \ \langle\varepsilon^k\rangle_2 \ \ \ldots \ \ \langle\varepsilon^k\rangle_6\right], & \text{if } a = b \\ [0 \ \ 0 \ \ 0 \ \ 0 \ \ 0 \ \ 0], & \text{if } a \neq b \end{cases}, \tag{68}$$

or in matrix representation:

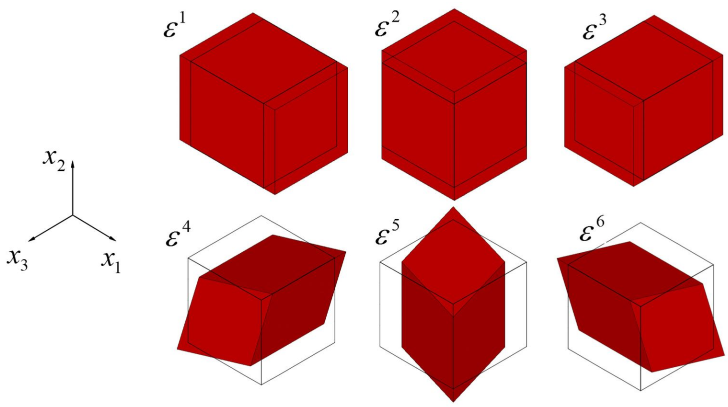

Figure 8: Visualization of the strain states ε^i in eqs. (65) for the particular case of constant strains.

$$\mathbf{M}^k_{ab} = \begin{bmatrix} \langle \varepsilon^k \rangle_{1\times 6} & [0]_{1\times 6} & \cdots & \cdots & \cdots & [0]_{1\times 6} \\ [0]_{1\times 6} & \langle \varepsilon^k \rangle_{1\times 6} & [0]_{1\times 6} & \cdots & \cdots & [0]_{1\times 6} \\ \vdots & [0]_{1\times 6} & \langle \varepsilon^k \rangle_{1\times 6} & [0]_{1\times 6} & \cdots & [0]_{1\times 6} \\ \vdots & \vdots & [0]_{1\times 6} & \langle \varepsilon^k \rangle_{1\times 6} & [0]_{1\times 6} & [0]_{1\times 6} \\ \vdots & \vdots & \vdots & [0]_{1\times 6} & \langle \varepsilon^k \rangle_{1\times 6} & [0]_{1\times 6} \\ [0]_{1\times 6} & [0]_{1\times 6} & [0]_{1\times 6} & [0]_{1\times 6} & [0]_{1\times 6} & \langle \varepsilon^k \rangle_{1\times 6} \end{bmatrix} . \tag{69}$$

Redundant equations can possibly be eliminated to account for the various symmetries of $\bar{\mathbf{C}}$. Alternatively, constraints can be used as well. The engineering constants can now be retrieved by inverting the stiffness matrix obtained by the solution of eq. (67), $\bar{\mathbf{S}} = \bar{\mathbf{C}}^{-1}$ as follows:

$$\bar{\mathbf{S}} = \begin{bmatrix} 1/E_1 & -\nu_{21}/E_2 & -\nu_{31}/E_3 & \eta_{1,23}/G_{23} & \eta_{1,13}/G_{13} & \eta_{1,12}/G_{12} \\ -\nu_{12}/E_1 & 1/E_2 & -\nu_{32}/E_3 & \eta_{2,23}/G_{23} & \eta_{2,13}/G_{13} & \eta_{2,12}/G_{12} \\ -\nu_{13}/E_1 & -\nu_{23}/E_2 & 1/E_3 & \eta_{3,23}/G_{23} & \eta_{3,13}/G_{13} & \eta_{3,12}/G_{12} \\ \eta_{23,1}/E_1 & \eta_{23,2}/E_2 & \eta_{23,3}/E_3 & 1/G_{23} & \mu_{23,13}/G_{13} & \mu_{23,12}/G_{12} \\ \eta_{13,1}/E_1 & \eta_{13,2}/E_2 & \eta_{13,3}/E_3 & \mu_{13,23}/G_{23} & 1/G_{13} & \mu_{13,12}/G_{12} \\ \eta_{12,1}/E_1 & \eta_{12,2}/E_2 & \eta_{12,3}/E_3 & \mu_{12,23}/G_{23} & \mu_{12,13}/G_{13} & 1/G_{12} \end{bmatrix} . \tag{70}$$

4.1 Fiber volume correction

In computational modeling of a textile composite, it is common to allow a thin layer of matrix material on the top and bottom sides of the RVE, as shown in fig. 9). This measure helps to avoid mesh generation issues (see, for instance, Long and Brown [2011]). As a result, the actual fiber volume fraction of the computational model is lowered and the homogenization process is affected. To correct this effect, Barbero's methodology (Barbero et al. [2006]) is followed in this work.

The correction is based on three fiber volume fractions: the overall, the mesoscale, and the tow fraction, denoted as V_o, V_g, and V_s, respectively. V_o is the ratio between the dry fiber volume and total (after curing) composite volume. The V_g measure is defined as the volume occupied by the strands with impregnated resin in the cured composite, or alternatively, in the computational representation of the tows. Finally, V_s is the volume fraction inside the strand. V_s is generally high (larger than 0.8), however, it is hard to be obtained experimentally. Barbero et al. [2006] introduce the following relationships among the volume fractions:

$$V_s = \frac{V_0}{V_g} . \tag{71}$$

V_g is obtained computationally while the V_o is an experiment value expected to be known. Furthermore, Barbero et al. [2006] suggest the following volume fraction correction for the Young modulus:

$$E = \frac{V_g}{V_g^{\alpha}} E^{\alpha} ; \tag{72}$$

with the superscript α meaning the value in the FEM model. Aiming at analyzing the stiffness matrix altogether, this correction is applied over the reduced constitutive tensor:

$$\bar{\mathbf{C}} = \frac{V_g}{V_g^{\alpha}}\,\bar{\mathbf{C}}^{\alpha}\,. \tag{73}$$

The approach is straightforward and corrects undesired effects on the final homogenized tensor. The issues do not appear in experimental values validation, since only common engineering constants are generally corrected and they are obtained from the main diagonal of the compliance tensor. Thus, caution is advisable when interpreting coupling coefficients. A deeper investigation of this correction and its influence on the stiffness/compliance tensors is out of the scope of this text.

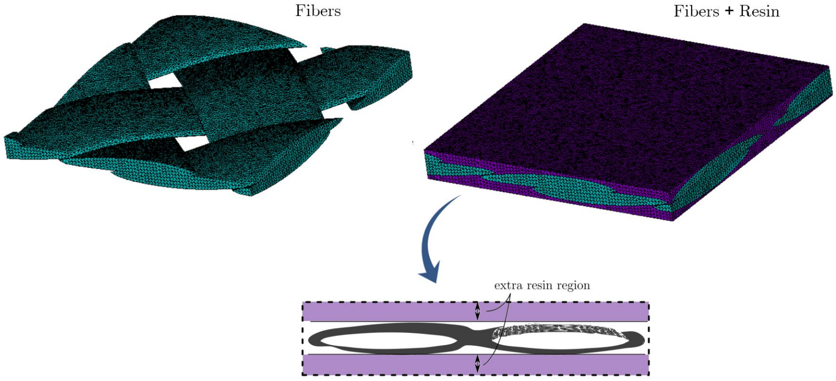

Figure 9: Typical extra layer of resin added by computational tools.

4.2 Principal directions of anisotropy

Rand and Rovenski [2007] introduced a straightforward methodology for defining the principal directions of an anisotropic material based on a bulk modulus tensor and a deviatoric modulus tensor. These are also contractions of the stiffness tensor, and are given by the following definitions:

- Bulk modulus tensor

$$\mathbf{K} = \begin{bmatrix} K_{11} & K_{12} & K_{13} \\ K_{12} & K_{22} & K_{23} \\ K_{13} & K_{23} & K_{33} \end{bmatrix}, \qquad K_{ij} = \sum_{k=1}^{3} S_{ijkk}\,. \tag{74}$$

- Deviatoric modulus tensor

$$\mathbf{L} = \begin{bmatrix} L_{11} & L_{12} & L_{13} \\ L_{12} & L_{22} & L_{23} \\ L_{13} & L_{23} & L_{33} \end{bmatrix}, \qquad L_{ij} = \sum_{k=1}^{3} S_{ikjk}\,. \tag{75}$$

The principal directions of $\mathbf{K}$ coincide with the principal directions of anisotropy of the material. In order to ensure a canonical system, the eigenvalues λ_i^K of $\mathbf{K}$ (or λ_i^L of $\mathbf{L}$) must be ordered $\lambda_3^K > \lambda_2^K > \lambda_1^K$, so that the *strongest* material direction will be oriented in the 3-axis, while the and the weakest remains in the 1-axis. Furthermore, a necessary (but not sufficient) condition for two materials to be considered the same is the invariants of $\mathbf{K}$ and $\mathbf{L}$ being the same. Consequently, the eigenvalues of these tensors can develop a suitable metric to compare the effects of the distinct boundary conditions on the homogenization results. There are a total of six invariants are associated with $\mathbf{K}$ and $\mathbf{L}$ tensors that can be used for expedite comparisons between two anisotropic materials. They are written as follows:

$$
\begin{aligned}
I_1^K &= \lambda_1^K + \lambda_2^K + \lambda_3^K & I_1^L &= \lambda_1^L + \lambda_2^L + \lambda_3^L \\
I_2^K &= \lambda_1^K\lambda_2^K + \lambda_1^K\lambda_3^K + \lambda_2^K\lambda_3^K & I_2^L &= \lambda_1^L\lambda_2^L + \lambda_1^L\lambda_3^L + \lambda_2^L\lambda_3^L \\
I_3^K &= \lambda_1^K\lambda_2^K\lambda_3^K & I_3^L &= \lambda_1^L\lambda_2^L\lambda_3^L
\end{aligned}
$$

5 Numerical Results

In this section, several results obtained through homogenization considering the boundary conditions described in the present chapter will be presented and discussed for a set of selected composites. For each case (composite + boundary condition set), the homogenized stiffness matrix is determined. Some metrics using these tensors are calculated so as to allow a better analysis of the differences that each set of boundary conditions may produce.

In view of the over-determined system of eq. (67) and the numerical nature of its solution, the $\bar{\mathbf{C}}$ tensor may not result perfectly symmetric. This was avoided by enforcing its symmetry before calculating other results, that is:

$$
\bar{\mathbf{S}}^{-1} = \bar{\mathbf{C}} \doteq \frac{1}{2}(\bar{\mathbf{C}}^{\mathrm{T}} + \bar{\mathbf{C}}) \;, \tag{76}
$$

Some indices are determined as a direct comparison among the resulting $\bar{\mathbf{C}}$ would be cumbersome and not quite objective. Therefore, the present work used the following indicators to compare the different stiffnesses:

1. Two anisotropy indices: the universal elastic anisotropy index (A_u), and Zener's anisotropy index (A_z) following Ranganathan and Ostoja-Starzewski [2008];

2. The Frobenius norm of the stiffness matrix;

3. The invariants of $\mathbf{K}$ and $\mathbf{L}$, regarding the principal planes of anisotropy (subsection 4.2);

4. Classical Laminate Theory (CLT) comparison through the reduced constitutive tensor (de Vargas Lisbôa and Marczak [2017]);

The universal elastic anisotropy index (A_u), the Zener's anisotropy index (A_z), and the Frobenius norm (F_r) are calculated as follows:

$$A_u(\bar{\mathbf{C}}) = 5\frac{G^V}{G^R} + \frac{K^V}{K^R} - 6 \ , \tag{77}$$

where

$$\begin{aligned} 9K_v &= (\bar{C}_{11} + \bar{C}_{22} + \bar{C}_{33} + 2(\bar{C}_{12} + \bar{C}_{23} + \bar{C}_{13}) \ , \\ 15G_v &= (\bar{C}_{11} + \bar{C}_{22} + \bar{C}_{33}) - (\bar{C}_{12} + \bar{C}_{23} + \bar{C}_{13}) + 3(\bar{C}_{44} + \bar{C}_{55} + \bar{C}_{66}) \end{aligned} \ , \tag{78}$$

and

$$A_z(\bar{\mathbf{C}}) = \frac{2\bar{C}_{44}}{\bar{C}_{11} - \bar{C}_{12}} \ , \tag{79}$$

$$F_r(\bar{\mathbf{C}}) = \sqrt{\mathrm{tr}(\bar{\mathbf{C}}\bar{\mathbf{C}})} \ . \tag{80}$$

For comparisons with CLT, eq. (3) is used. Given the kinematic assumptions of thin plate theory and $\sigma_{33} = 0$, a reduction of the 6 × 6 constitutive tensor can be derived by adjusting the remaining stiffnesses as follows:

$$\bar{\bar{C}}_{ij} = C_{IJ} - \frac{C_{I3}C_{3J}}{C_{33}} \ , \tag{81}$$

where $\{I, J\} = \{1, 2, 6\}$ and $I = i + \max{(3(i-2), 0)}$, the later also valid when upper and lower i are replaced for j. Evidently, $\bar{\bar{\mathbf{C}}} = \bar{\bar{\mathbf{S}}}^{-1}$.

The results section will be divided into two sections. In the first one, one studies a simple $[0/90]_s$ cross-ply laminate and uses the advantage of its simplicity to analyze it under the context of the CLT. In the second section textile composites manufactured with typical weaving will be analyzed and compared with experimental results from the literature [Scida et al., 1998]. In order to calculate A_u, A_z, and F_r from experimental data to be used as reference values, the compliance matrix is calculated from eq. (70) using the measured engineering constants.

The mechanical and the geometric properties of the composites analyzed throughout this section are listed in tables 1 and 2, respectively.

Table 1: Material properties used.

Material	E_{11} (MPa)	E_{22} (MPa)	G_{12} (MPa)	G_{23} (MPa)	ν_{12}	ν_{23}
E-glass	73	73	30.4	30.4	0.2	0.2
Epoxy	3.2	3.2	1.16	1.16	0.38	0.38
Vinylester derakane	3.4	3.4	1.49	1.49	0.35	0.35
E-glass/Vinylester, $V_s = 0.8$	57.5	18.8	7.44	7.26	0.25	0.29
E-glass/Epoxy, $V_s = 0.8$	59.3	23.2	8.68	7.60	0.21	0.32
E-glass/Epoxy, $V_s = 0.75$	55.7	18.5	6.89	6.04	0.22	0.34

Table 2: Geometric properties of the analyzed composites.

Material		E-glass/Vinylester	E-glass/Vinylester	E-glass/Epoxy	E-glass/Epoxy
Weave class		$[0/90]_s$	Plain weave	2/2 twill weave	8-harness satin
Strand width (mm)		0.20	0.60	0.83	0.60
Strand thickness (mm)		0.20	0.05	0.09	0.09
Unit-cell thickness (mm)		0.88	0.10	0.2275	0.18
FVF[†]	Strand (V_s)	1.00	0.80	0.75	0.80
	Composite (V_o)	0.26	0.55	0.38	0.52
	Meso-Scale (V_m)	0.26	0.687	0.507	0.65

[†] Fiber volume fraction

5.1 Cross-ply laminates

In this section, results for the $[0/90]_s$ cross-ply laminate (see figure 10) are discussed. The material and geometric properties used in this case are listed in tables 1 and 2, respectively. Since the geometry of the problem was generated in the TexGen software [Lin et al., 2011, Long and Brown, 2011], the input parameters of TexGen are shown in table 3, for the sake of reproducibility.

Table 3: TexGen weave parameters for the top layers of the $[0/90]_s$ cross-ply laminate.

Material	N. Layers	Warp/Weft Yarns	Yarn Spacing (mm)	Yarn Width (mm)	Fabric. thk.
E-glass/Epoxy	2	5	0.5	0.2	0.4

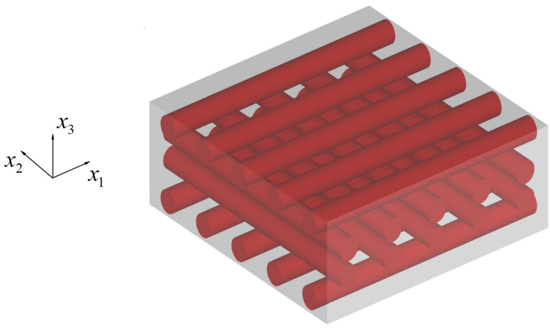

Figure 10: Simplified $[0/90]_s$ cross-ply laminate.

5.1.1 Homogenized stiffness

The $\bar{\mathrm{C}}$ matrix evaluated for each case of boundary conditions discussed in sections 2.2.2 and 3, namely SUBC and PBC, will be herein referenced by the corresponding superscripts. The proposed set of mixed boundary conditions described in section 3, MBC*, will be assessed in the context of both, the 3D $\bar{\mathrm{C}}$ and thin structures such as plate/shell using $\bar{\bar{\mathrm{C}}}$. Therefore, the raw results of the symmetrized stiffness obtained for the cross-ply $[0/90]_S$ laminate are:

$$\bar{\mathbf{C}}^{SUBC} = \begin{bmatrix} 15525.50 & 3256.47 & 3585.68 & 0.70 & 0.03 & -0.01 \\ 3315.44 & 15426.91 & 3612.21 & 0.61 & 0.07 & 0.01 \\ 3585.76 & 3485.87 & 9505.93 & 0.35 & -0.03 & -0.01 \\ 1.43 & 0.25 & 0.23 & 2307.38 & -0.01 & -0.02 \\ -0.01 & 0.10 & -0.06 & -0.01 & 2671.86 & 0.17 \\ -0.01 & -0.01 & -0.01 & -0.04 & 0.48 & 2508.81 \end{bmatrix} , \quad (82a)$$

$$\bar{\mathbf{C}}^{PBC} = \begin{bmatrix} 15343.92 & 3240.38 & 3527.00 & 0.20 & 0.01 & -0.01 \\ 3240.34 & 15334.77 & 3527.50 & 0.18 & 0.00 & 0.01 \\ 3526.94 & 3527.50 & 9101.15 & 0.16 & -0.03 & -0.02 \\ 0.20 & 0.18 & 0.16 & 1944.53 & 0.01 & -0.00 \\ 0.00 & 0.00 & -0.03 & 0.01 & 2255.10 & 0.12 \\ -0.00 & 0.01 & -0.02 & -0.00 & 0.12 & 2255.68 \end{bmatrix} , \quad (82b)$$

$$\bar{\mathbf{C}}^{MBC^{*}} = \begin{bmatrix} 15351.59 & 3238.43 & 3548.45 & 0.20 & 0.02 & -0.01 \\ 3238.39 & 15342.42 & 3548.96 & 0.17 & 0.02 & 0.00 \\ 3548.39 & 3548.95 & 9425.97 & 0.15 & -0.03 & -0.03 \\ 0.20 & 0.17 & 0.15 & 1944.53 & 0.01 & -0.00 \\ -0.00 & 0.00 & -0.06 & 0.01 & 2352.61 & 0.18 \\ -0.01 & 0.01 & -0.03 & -0.00 & 0.43 & 2306.12 \end{bmatrix} . \quad (82c)$$

5.1.2 3D anisotropy and engineering constants

Once the homogenized, matrices given by eqs. (82) are generated, the anisotropy indicators are computed along with the engineering constants for comparison purposes. Table 4 summarizes these calculations for an E-glass/vinylester cross-ply laminate.

Table 4: Cross-ply E-glass/vinylester composite

b.c.	E_{11}	E_{22}	E_{33}	ν_{13}	ν_{12}	A_u	A_z	F_r
SUBC	13.9	13.8	8.15	0.32	0.138	1.53	0.437	25703.14
MBC*	13.8	13.7	8.07	0.32	0.136	1.84	0.388	25414.39
PBC	13.7	13.7	7.76	0.33	0.134	1.94	0.373	25261.47

If the F_r norm is considered, and assuming it can give us at least a weak indication of the composite stiffness, the results in Table 4 shows that:

$$F_r\left(\bar{\mathbf{C}}^{SUBC}\right) > F_r\left(\bar{\mathbf{C}}^{MBC^{*}}\right) > F_r\left(\bar{\mathbf{C}}^{PBC}\right) . \quad (83)$$

Espadas-Escalante et al. [2017] conducted a similar study with a mixed boundary condition consisting of a combination of the PBC and the uniform traction boundary conditions (UTBC), here referred to as MBC**. The results showed that:

$$F_r\left(\bar{\mathbf{C}}^{SUBC}\right) > F_r\left(\bar{\mathbf{C}}^{PBC}\right) > F_r\left(\bar{\mathbf{C}}^{MBC^{**}}\right) > F_r\left(\bar{\mathbf{C}}^{UTBC}\right) , \quad (84)$$

suggesting that the MBC** combination of UTBC and PBC produced a resulting $\bar{\mathbf{C}}$ stiffer than $\bar{\mathbf{C}}^{UTBC}$. On the other hand, our MBC* proposal, combining SUBC and PBC, produced a $\bar{\mathbf{C}}$ less stiff than $\bar{\mathbf{C}}^{SUBC}$. These conclusions highlight that combinations of distinct boundary conditions have the potential to represent better actual stiffness, as these combinations allow the generation of intermediary strain fields, particularly for more complex fiber distributions.

The PBC infers a 3D infinite domain. Despite being valid for large 3D bodies, in textile composites or shell-like geometries this set might not be accurate in the out-of-plane direction. Furthermore, the SUBC imposes a direct strain state along the boundary, which can be seen as an upper bound limit of the elastic properties. Consequently, one expects that the MBC should generate results with intermediary stiffness between the SUBC and the PBC.

Table 5 presents a comparison between the I_i^K and I_i^L for the boundary conditions sets evaluated. As mentioned in section 4.2, a necessary condition to claim that two anisotropic materials behave identically is that their invariants I_i^K and I_i^L must be equal. This implies that the main planes of anisotropy have the same spatial orientation. Table 5 shows clearly that the three sets of boundary conditions generate similar results. The small differences appear to be a consequence of the local strain fields generated in the boundary condition application, which is also reflected in the numerical values of the engineering constants (Table 4).

Table 5: Invariants of K and L for the cross-ply E-glass/vinylester composite.

b.c.	I_1^K	I_2^K	I_3^K	I_1^L	I_2^L	I_3^L
SUBC	6.13×10^4	1.24×10^9	8.30×10^{12}	5.54×10^4	10.1×10^9	6.05×10^{12}
MBC*	6.08×10^4	1.22×10^9	8.10×10^{12}	5.33×10^4	9.35×10^9	5.37×10^{12}
PBC	6.04×10^4	1.20×10^9	7.90×10^{12}	5.27×10^4	9.12×10^9	5.16×10^{12}

A direct comparison of other 3D homogenized compliance entries is presented in Table 6 for completeness. In particular, values for out-of-plane compliance are provided for reference, as these are not commonly found in the literature.

Table 6: Other entries for 3D homogenized compliance

Model	$\bar{S}_{13}$	$\bar{S}_{32}$	$\bar{S}_{63}$	$\bar{S}_{12}$	$\bar{S}_{33}$	$\bar{S}_{66}$
SUBC	$-2.34 \cdot 10^{-5}$	$-2.32 \cdot 10^{-5}$	$-2.67 \cdot 10^{-10}$	$-9.93 \cdot 10^{-6}$	$1.23 \cdot 10^{-4}$	$4.33 \cdot 10^{-4}$
MBC*	$-2.36 \cdot 10^{-5}$	$-2.37 \cdot 10^{-5}$	$-4.79 \cdot 10^{-9}$	$-9.87 \cdot 10^{-6}$	$1.24 \cdot 10^{-4}$	$5.14 \cdot 10^{-4}$
PBC	$-2.44 \cdot 10^{-5}$	$-2.45 \cdot 10^{-5}$	$-5.54 \cdot 10^{-9}$	$-9.77 \cdot 10^{-6}$	$1.29 \cdot 10^{-4}$	$5.14 \cdot 10^{-4}$

5.1.3 2D anisotropy and engineering constants

After reducing the $\bar{\mathbf{C}}^{SUBC}$, $\bar{\mathbf{C}}^{PBC}$, and $\bar{\mathbf{C}}^{MBC^*}$ homogenized matrices (eq. (81)), their CLT counterparts are obtained as follows:

$$\bar{\bar{\mathbf{C}}}^{SUBC} = \begin{bmatrix} 14172.94 & 1947.22 & 0.96 \\ 1947.22 & 14101.87 & 0.32 \\ 0.96 & 0.32 & 2307.38 \end{bmatrix} \tag{85a}$$

$$\bar{\bar{\mathbf{C}}}^{MBC^*} = \begin{bmatrix} 14015.78 & 1902.40 & 0.15 \\ 1902.40 & 14006.21 & 0.12 \\ 0.15 & 0.12 & 1944.53 \end{bmatrix} \tag{85b}$$

$$\bar{\bar{\mathbf{C}}}^{PBC} = \begin{bmatrix} 13977.11 & 1873.35 & 0.14 \\ 1873.35 & 13967.55 & 0.12 \\ 0.14 & 0.12 & 1944.53 \end{bmatrix} \tag{85c}$$

It is worth highlighting that the tensor reduction disregards the following entries of the homogenized 3D stiffness matrix due to the kinematic hypotheses of Kirchhoff plate theory:

$$\begin{bmatrix} C_{11} & C_{12} & C_{13} & C_{14} & C_{15} & C_{16} \\ C_{21} & C_{22} & C_{23} & C_{24} & C_{25} & C_{26} \\ C_{31} & C_{32} & C_{33} & C_{34} & C_{35} & C_{36} \\ C_{41} & C_{42} & C_{43} & C_{44} & C_{45} & C_{46} \\ C_{51} & C_{52} & C_{53} & C_{56} & C_{55} & C_{56} \\ C_{61} & C_{62} & C_{63} & C_{64} & C_{65} & C_{66} \end{bmatrix} \tag{86}$$

Consequently, some of the entries in eqs. (82) responsible for the asymmetry are not considered.

It is interesting to note that one can retrieve the effective engineering constants for the composite either from the inverse of eq. (70) combined with any of the eqs. (82) or, alternatively, from the elementary relations of mechanics of composite materials (Jones [2018], Nettles [1994]), fed by the inverses of the eqs. (85). In both cases, the equations are the same, provided the $\{I, J\} \rightarrow \{i, j\}$ index change is performed and the correct matrices are used. Therefore, to retrieve the effective properties from the CLT (reduced) matrices, we have:

$$\begin{aligned} E_{11} &= \frac{1}{\bar{\bar{S}}_{11}} & E_{22} &= \frac{1}{\bar{\bar{S}}_{22}} \\ G_{12} &= \frac{1}{\bar{\bar{S}}_{33}} & \nu_{12} &= -\frac{\bar{\bar{S}}_{12}}{\bar{\bar{S}}_{22}} \end{aligned} \tag{87}$$

In Table 7, the effective properties are computed from eqs. (87) using $\bar{\bar{S}}_{ij}$ from the inverses (85) are compared. The ROM acronym refers to the values obtained using the rule of mixtures (Jones [2018], Nettles [1994]). It is clear that the different calculations of the reduced stiffness matrix produced a consistent agreement for the elastic moduli. Another comparison of the values in Table 7 is provided in fig. 11, where E_{11} of the various formulations are plotted along with the bounds described in section 2.1.1. One observes that for a cross-ply laminate ($N = 2$) the homogenized values agree with the upper bound of Ishikawa [1981].

Table 7: Effective engineering constants for cross-ply E-glass/vinylester composite.

b.c.	E_{11}	E_{22}	G_{12}	ν_{12}
SUBC	13.90	13.83	2.307	0.1374
MBC*	13.76	13.75	1.945	0.1357
PBC	13.73	13.72	1.945	0.1340
ROM	13.39	13.39	2.05	0.118

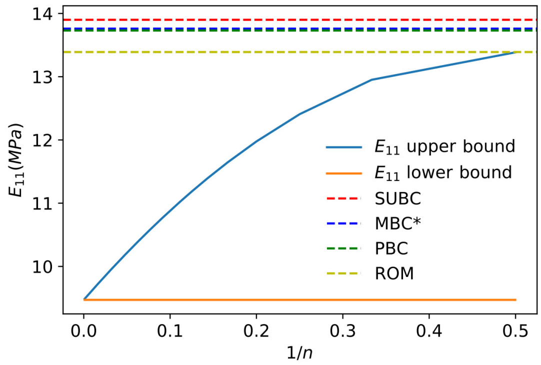

Figure 11: Comparison of the elastic moduli obtained by the various formulations and the bounds proposed by Ishikawa [1981].

5.2 Textile composites

In this section, the homogenization process is conducted for some weave composites typically found in the industry. The geometry was also generated in a commercial textile composites simulation software (TexGen) and the results are compared to experimental and numerical evaluations from literature. Later, the homogenized stiffness matrix is reduced to CLT and also compared. The cases are analyzed and the corresponding fiber volume fractions are:

1. Plain Weave E-glass/Vinylester ($V_s = 0.8$);
2. 2/2 twill weave E-glass/Epoxy ($V_s = 0.75$)
3. 8-Harness Satin Weave E-glass/Epoxy ($V_s = 0.8$)

The weave patterns studied are diagrammed in fig. 12 and the corresponding geometries generated by TexGen are shown in fig. 13. The weaving parameters used to generate these models are listed in Table 8 and were retrieved from Scida et al. [1999]. The stiffness matrices were corrected in order to simulate the real fiber volume fraction of the composite, as described in section 4.1, eq. (73).

Table 8: TexGen input parameters used.

Material	Weave class	Strand width (mm)	Comp. thickness (mm)	Yarn Spacing (mm)	V_g^α	V_g/V_g^α
E-glass/Vinylester	Plain weave	0.6	0.1	0.625	0.589	1.165
E-glass/Epoxy	2/2 twill weave	0.83	0.2275[†]	1	0.498	1.017
E-glass/Epoxy	8-Harness Satin Weave	0.6	0.18	0.8	0.526	1.235

[†] The total thickness of the composite is 0.2275 mm. However, the fabric thickness which is actually inserted in TexGen is 0.18 mm. Hence, the fabric thickness is corrected by adding an additional layer of matrix material.

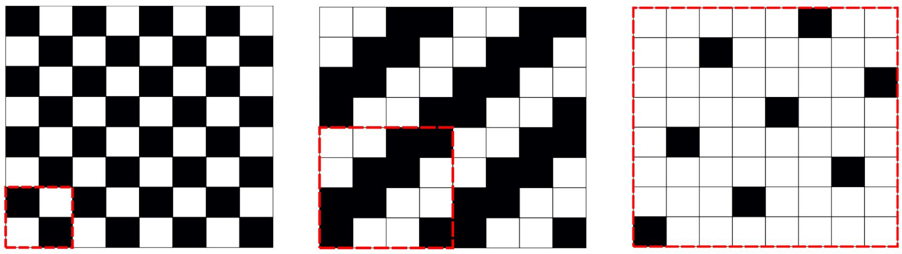

(a) Plain Weave (b) 2/2 twill weave (c) 8-Harness Satin Weave

Figure 12: Weave pattern schemes used to generate the three weave composites studied.

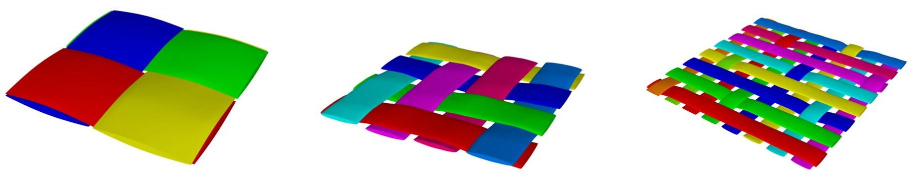

(a) Plain Weave (b) 2/2 twill weave (c) 8-Harness Satin Weave

Figure 13: RVE geometries generated for each pattern of Fig. 12.

5.2.1 Homogenized stiffness

In this subsection, the 3D homogenized (non-contracted) stiffness matrix computed for each of the three textile composites will be discussed. For short, they will be distinguished by their names attached to the $\bar{\mathbf{C}}$ matrix. They are:

$$\bar{\mathbf{C}}_{\text{plain}}^{SUBC} = \begin{bmatrix} 28874.13 & 6117.78 & 6305.27 & -18.19 & -481.47 & 732.65 \\ 6478.04 & 29131.20 & 6312.37 & 759.37 & 1.27 & -4.18 \\ 6305.42 & 5584.47 & 13194.71 & 12.05 & -0.56 & 18.27 \\ -47.26 & 634.76 & 0.54 & 2721.56 & 5.10 & -10.19 \\ -481.44 & -1.84 & -0.59 & 2.74 & 2983.75 & -17.24 \\ 988.30 & -9.13 & 26.10 & -7.48 & -31.46 & 4775.66 \end{bmatrix} \tag{88a}$$

$$\bar{\mathbf{C}}_{\text{plain}}^{PBC} = \begin{bmatrix} 28331.60 & 6452.85 & 6197.92 & -30.53 & -457.13 & 957.37 \\ 6453.30 & 28634.90 & 6211.23 & 465.35 & -4.90 & 7.81 \\ 6197.87 & 6210.75 & 13084.94 & 0.92 & -0.58 & 30.03 \\ -30.52 & 465.35 & 0.93 & 2772.56 & 1.67 & -10.37 \\ -457.13 & -4.90 & -0.58 & 1.67 & 2771.43 & -30.76 \\ 957.37 & 7.83 & 30.05 & -10.38 & -30.76 & 4876.75 \end{bmatrix} \tag{88b}$$

$$\bar{\mathbf{C}}_{\text{plain}}^{MBC^*} = \begin{bmatrix} 28433.07 & 6382.58 & 6218.58 & -12.93 & -425.32 & 965.06 \\ 6382.95 & 28736.06 & 6231.57 & 540.20 & 1.89 & 2.27 \\ 6218.54 & 6231.17 & 13149.13 & 2.16 & 2.04 & 29.91 \\ -41.71 & 432.58 & -1.67 & 2450.17 & 1.75 & -12.08 \\ -425.34 & 1.89 & 2.02 & 0.84 & 2892.14 & -25.63 \\ 965.06 & 2.27 & 29.92 & -6.21 & -25.63 & 4877.89 \end{bmatrix} \tag{88c}$$

for the plain weave;

$$\bar{\mathbf{C}}_{\text{twill}}^{SUBC} = \begin{bmatrix} 22170.91 & 4914.31 & 5076.26 & -5.64 & -194.87 & 289.69 \\ 5192.57 & 22055.12 & 5080.02 & 311.95 & 0.86 & -7.25 \\ 5075.87 & 4633.46 & 10108.11 & 4.63 & 0.37 & 10.33 \\ -17.74 & 261.84 & -0.20 & 2076.20 & 5.42 & -2.96 \\ -194.42 & -2.72 & 0.26 & 2.48 & 2224.88 & -3.69 \\ 418.73 & -12.08 & 15.33 & -1.86 & -10.68 & 3470.17 \end{bmatrix} \tag{89a}$$

$$\bar{\mathbf{C}}_{\text{twill}}^{PBC} = \begin{bmatrix} 21837.35 & 5160.93 & 5015.48 & -13.78 & -188.56 & 398.70 \\ 5160.86 & 21993.03 & 5020.53 & 189.97 & 0.77 & -8.24 \\ 5014.96 & 5020.10 & 10029.43 & 0.31 & -0.19 & 15.17 \\ -13.77 & 189.98 & 0.32 & 2090.10 & 2.94 & -3.50 \\ -188.57 & 0.76 & -0.20 & 2.94 & 2089.89 & -9.37 \\ 398.71 & -8.23 & 15.19 & -3.50 & -9.37 & 3504.09 \end{bmatrix} \tag{89b}$$

$$\bar{\mathbf{C}}_{\text{twill}}^{MBC^*} = \begin{bmatrix} 21915.77 & 5121.05 & 5028.02 & -6.63 & -178.92 & 402.97 \\ 5120.99 & 22076.02 & 5033.40 & 220.81 & 3.25 & -9.55 \\ 5027.62 & 5033.08 & 10078.52 & 2.14 & 0.85 & 16.21 \\ -18.22 & 180.12 & -0.64 & 1870.07 & 3.05 & -4.16 \\ -178.93 & 3.22 & 0.77 & 2.11 & 2155.16 & -7.72 \\ 402.99 & -9.54 & 16.22 & -1.93 & -7.72 & 3505.08 \end{bmatrix} \tag{89c}$$

for the 2/2 twill weave, and

$$\bar{\mathbf{C}}_{\text{satin}}^{SUBC} = \begin{bmatrix} 27304.15 & 5970.20 & 6365.65 & -10.42 & -157.92 & 202.39 \\ 6286.58 & 27858.86 & 6370.29 & 239.53 & -0.02 & 4.42 \\ 6364.15 & 5909.39 & 12948.78 & 5.73 & -1.05 & 7.11 \\ -17.03 & 179.75 & 0.00 & 2786.00 & 1.67 & -3.91 \\ -157.59 & -0.62 & -0.14 & 0.78 & 2940.36 & -12.73 \\ 293.66 & -1.20 & 9.81 & -2.32 & -10.03 & 4159.94 \end{bmatrix} \tag{90a}$$

$$\bar{\mathbf{C}}_{\text{satin}}^{PBC} = \begin{bmatrix} 26809.47 & 6210.06 & 6264.62 & -11.56 & -158.35 & 269.87 \\ 6211.52 & 26985.12 & 6273.02 & 161.25 & -1.54 & 2.28 \\ 6259.36 & 6266.59 & 12817.02 & 1.49 & -1.49 & 10.61 \\ -11.37 & 162.08 & 1.63 & 2685.45 & 0.51 & -2.77 \\ -158.34 & -1.56 & -1.54 & 0.51 & 2684.54 & -8.53 \\ 269.90 & 2.32 & 10.66 & -2.77 & -8.58 & 3992.46 \end{bmatrix} \tag{90b}$$

$$\bar{\mathbf{C}}_{\text{satin}}^{MBC^*} = \begin{bmatrix} 26899.39 & 6179.88 & 6285.15 & -15.72 & -151.36 & 274.57 \\ 6181.20 & 27078.99 & 6294.05 & 85.15 & 1.01 & 1.05 \\ 6281.49 & 6289.15 & 12902.98 & 7.00 & -0.82 & 10.68 \\ -16.82 & 155.13 & -0.10 & 2430.36 & 0.62 & -3.52 \\ -151.82 & 1.04 & 0.11 & 0.46 & 2843.23 & -6.85 \\ 274.58 & 1.07 & 10.72 & -0.88 & -6.92 & 3993.26 \end{bmatrix} \tag{90c}$$

for the 8-harness satin weave.

5.2.2 3D anisotropy, engineering constants, and comparison with literature

At this point, having the 3D $\bar{\mathbf{C}}$ matrix for each weave pattern as given by eqs. (88)-(90), the effective material properties can be computed, as well as the anisotropy indicators. Without the imposition of any type of constraints, as implemented here, the $\bar{\mathbf{C}}$ matrices are allowed to result fully anisotropic. That is, no effort was made to try to frame the resulting matrices into any specific material symmetry. Tables 9, 10, and 11 list all 9 effective material properties so obtained for the three weave composites under each type of boundary condition, as well as similar values from the literature, when available. In Tables 10 and 11, the starred values come from the analytical calculations of Scida et al. [1999], not experimental values.

Table 12 summarizes the anisotropy indicators for all three weave composites subjected to each of the three boundary conditions studied. Finally, Tables 13, 14, and 15 list the calculations of the invariants of $\mathbf{K}$ and $\mathbf{L}$ for each weave pattern. The effective engineering constants are compiled in Tables 13, 14, and 15 for each textile analyzed.

Table 9: Effective material properties comparison for E-glass/vinylester plain-weave composite.

b.c	E_1	E_2	E_3	G_{12}	G_{23}	G_{31}	ν_{13}	ν_{23}	ν_{12}
SUBC	25.18	25.81	11.06	4.74	2.70	2.97	0.42	0.35	0.13
PBC	24.66	25.12	10.87	4.84	2.76	2.76	0.41	0.41	0.13
MBC*	24.78	25.52	10.92	4.84	2.44	2.88	0.41	0.41	0.13
Barbero et al. [2006]	24.44	24.53	10.25	5.51	3.15	3.16	0.38	0.38	0.13
Scida et al. [1999]	24.8	24.8	8.5	6.5	4.2	4.2	0.28	0.28	0.11

Table 10: Effective material properties comparison for 2/2 twill E-glass woven fabric/epoxy composite.

b.c	E_1	E_2	E_3	G_{12}	G_{23}	G_{31}	ν_{13}	ν_{23}	ν_{12}
SUBC	19.92	19.93	8.29	3.46	2.07	2.22	0.44	0.39	0.13
PBC	18.91	19.10	8.17	3.50	2.01	2.01	0.43	0.43	0.14
MBC*	19.00	19.92	8.21	3.49	1.87	2.15	0.43	0.43	0.13
Scida et al. [1999]	19.2	19.2	10.92*	3.6	3.78*	3.78*	0.305*	0.305*	0.13

Table 13: Invariants of K and L for the plain weave composite.

b.c.	I_1^K	I_2^K	I_3^K	I_1^L	I_2^L	I_3^L
SUBC	1.08×10^5	3.82×10^9	4.36×10^{13}	9.22×10^4	2.76×10^9	2.65×10^{13}
PBC	1.08×10^5	3.79×10^9	4.31×10^{13}	9.09×10^4	2.68×10^9	2.55×10^{13}
MBC*	1.08×10^5	3.80×10^9	4.34×10^{13}	9.08×10^4	2.68×10^9	2.55×10^{13}

Table 14: Invariants of K and L for the 2/2 twill weave composite.

b.c.	I_1^K	I_2^K	I_3^K	I_1^L	I_2^L	I_3^L
SUBC	8.43×10^4	2.32×10^9	2.07×10^{13}	6.99×10^4	1.58×10^9	1.15×10^{13}
PBC	8.43×10^4	2.32×10^9	2.07×10^{13}	6.92×10^4	1.56×10^9	1.12×10^{13}
MBC*	8.44×10^4	2.33×10^9	2.08×10^{13}	6.91×10^4	1.55×10^9	1.12×10^{13}

Table 15: Invariants of K and L for the 8-harness satin weave composite.

b.c.	I_1^K	I_2^K	I_3^K	I_1^L	I_2^L	I_3^L
SUBC	1.06×10^5	3.65×10^9	4.09×10^{13}	8.81×10^4	2.52×10^9	2.32×10^{13}
PBC	1.04×10^5	3.56×10^9	3.95×10^{13}	8.55×10^4	2.38×10^9	2.12×10^{13}
MBC*	1.05×10^5	3.58×10^9	3.99×10^{13}	8.56×10^4	2.38×10^9	2.14×10^{13}

Table 11: Effective material properties comparison for E-glass eight-harness satin weave/epoxy composite.

b.c	E_1	E_2	E_3	G_{12}	G_{23}	G_{31}	ν_{13}	ν_{23}	ν_{12}
SUBC	23.81	24.59	10.65	4.16	2.79	2.94	0.44	0.39	0.13
PBC	23.36	23.54	10.47	3.99	2.69	2.69	0.42	0.42	0.13
MBC*	23.46	23.6	10.54	3.99	2.43	2.84	0.44	0.39	0.13
Scida et al. [1999]	25.6	25.6	15.65*	5.7	5.42*	5.42*	0.283*	0.283*	0.13

Table 12: Anisotropy indicators for the weave composites analyzed.

	Plain weave			2/2 twill weave			8-harness satin weave		
b.c.	A_u	A_z	F_r	A_u	A_z	F_r	A_u	A_z	F_r
SUBC	3.26	0.241	39597	3.24	0.243	34788	3.00	0.263	35800
PBC	3.22	0.253	39081	3.25	0.251	34578	3.05	0.261	35071
MBC*	3.40	0.222	39189	3.43	0.223	34678	3.14	0.235	35183

5.2.3 2D anisotropy and engineering constants

$$\bar{\bar{\mathbf{C}}}^{SUBC}_{\text{plain}} = \begin{bmatrix} 28874.13 & 6297.91 & 6305.35 \\ 6297.91 & 29131.20 & 5948.42 \\ 6305.35 & 5948.42 & 13194.71 \end{bmatrix} \tag{91a}$$

$$\bar{\bar{\mathbf{C}}}^{PBC}_{\text{plain}} = \begin{bmatrix} 28331.60 & 6453.07 & 6197.89 \\ 6453.07 & 28634.90 & 6210.99 \\ 6197.89 & 6210.99 & 13084.94 \end{bmatrix} \tag{91b}$$

$$\bar{\bar{\mathbf{C}}}^{MBC^*}_{\text{plain}} = \begin{bmatrix} 28433.07 & 6382.77 & 6218.56 \\ 6382.77 & 28736.06 & 6231.37 \\ 6218.56 & 6231.37 & 13149.13 \end{bmatrix} \tag{91c}$$

for the plain weave;

$$\bar{\bar{\mathbf{C}}}^{SUBC}_{\text{twill}} = \begin{bmatrix} 22170.91 & 5053.44 & 5076.07 \\ 5053.44 & 22055.12 & 4856.74 \\ 5076.07 & 4856.74 & 10108.11 \end{bmatrix} \tag{92a}$$

$$\bar{\bar{\mathbf{C}}}^{PBC}_{\text{twill}} = \begin{bmatrix} 21837.35 & 5160.93 & 5015.48 \\ 5160.86 & 21993.03 & 5020.53 \\ 5014.96 & 5020.10 & 10029.43 \end{bmatrix} \tag{92b}$$

$$\bar{\bar{\mathbf{C}}}^{MBC^*}_{\text{twill}} = \begin{bmatrix} 21915.77 & 5121.02 & 5027.82 \\ 5121.02 & 22076.02 & 5033.24 \\ 5027.82 & 5033.24 & 10078.52 \end{bmatrix} \tag{92c}$$

for the 2/2 twill weave, and

$$\bar{\bar{\mathbf{C}}}_{\text{satin}}^{SUBC} = \begin{bmatrix} 27304.15 & 6128.39 & 6364.90 \\ 6128.39 & 27858.86 & 6139.84 \\ 6364.90 & 6139.84 & 12948.78 \end{bmatrix} \tag{93a}$$

$$\bar{\bar{\mathbf{C}}}_{\text{satin}}^{PBC} = \begin{bmatrix} 26809.47 & 6210.79 & 6261.99 \\ 6210.79 & 26985.12 & 6269.80 \\ 6261.99 & 6269.80 & 12817.02 \end{bmatrix} \tag{93b}$$

$$\bar{\bar{\mathbf{C}}}_{\text{satin}}^{MBC^*} = \begin{bmatrix} 26899.39 & 6180.54 & 6283.32 \\ 6180.54 & 27078.99 & 6291.60 \\ 6283.32 & 6291.60 & 12902.98 \end{bmatrix} \tag{93c}$$

for the 8-harness satin weave, noting again that the symmetry was enforced before the reduction of the stiffness tensors.

Now the stiffness given in eqs. (91), (92), and (93) can be inverted to easily calculate the engineering constants in order to verify how our results compare with the ones obtained by Scida et al. [1999], as well as the value values obtained using ROM (Jones [2018], Nettles [1994]). The homogenized engineering constants are listed in Tables 16, 17, and 18. It is interesting to note that even properties not directly affected by the reduction $\bar{\mathbf{C}} \to \bar{\bar{\mathbf{C}}}$, such as E_{11}, change their values despite the expression for its evaluation being the same in both, 3D and CLT.

Table 16: Effective engineering constants for the plain weave composite.

b.c.	E_{11}	E_{22}	G_{12}	ν_{12}
UDBC	27.28	27.74	4.75	0.21
PBC	26.61	27.15	4.84	0.22
MBC*	26.76	27.29	4.84	0.22
ROM	27.18	27.18	4.05	0.11
Scida et al. [1999]	24.8 ±1.1	24.8 ±1.1	6.5 ±0.8	0.11 ±0.01

Table 17: Effective engineering constants for the 2/2 twill weave composite.

b.c.	E_{11}	E_{22}	G_{12}	ν_{12}
SUBC	20.96	20.33	3.46	0.22
PBC	20.56	20.76	3.49	0.23
MBC*	20.66	20.87	3.49	0.23
ROM	18.76	18.97	2.48	0.12
Scida et al. [1999]	19.2 ±1.1	19.2 ±1.1	3.6 ±0.1	0.13 ±0.005

Table 18: Effective engineering constants for the 8-harness satin weave composite.

b.c.	E_{11}	E_{22}	G_{12}	ν_{12}
UDBC	25.93	26.48	4.15	0.22
PBC	25.35	25.54	3.98	0.23
MBC*	25.46	25.66	3.99	0.23
ROM	25.74	25.74	3.74	0.12
Scida et al. [1999]	25.6 ± 0.2	25.6 ± 0.2	5.7 ± 0.3	0.13 ± 0.005

Finally, the same exercise made for the cross-ply laminate in fig. 11 can be repeated for all three textile composites, to visualize where E_{11} is placed relative to the analytical bounds described in section 2.1.1. These results are plotted in fig. 14. The textile composites analyzed here (plain, 2/2 twill, and 8-harness satin) do not have the same material/V_o combinations, and therefore the bounds, as well as the value predicted by ROM, are different for each one. It is clear, however, that the difference of moduli for the boundary conditions may reach 3-4%.

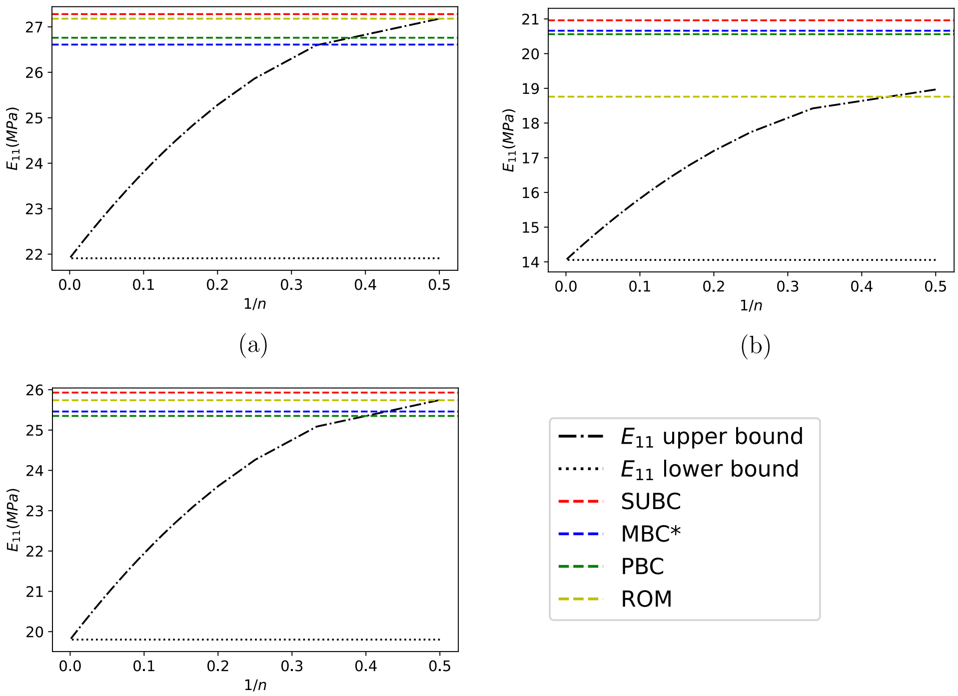

(a) (b) (c)

Figure 14: Comparison of the elastic moduli obtained by the various formulations and the bounds proposed by Ishikawa [1981] for (a) plain weave; (b) 2/2 twill weave, and (c) 8-harness satin weave.

5.3 Stress and strain fields

In order to provide an idea of how the different weave patterns influence the stress and strain distribution, figs. 15, 16, and 17 show the stress plot of these configurations for each boundary condition studied under ε^1 strain state. The finite element mesh of the matrix phase is not plotted for clarity. Only the σ_{13} component is shown, but it suffices to evidence how the patterns command differently the deformation mechanism of each composite. Although not shown here, patterns of composite with the same fiber/matrix material composition and fractions will respond differently, and the particularities of each deformation mode cannot be captured by average field theory approaches. RVE homogenization equipped with a proper set of boundary conditions seems to be the only method able to reproduce the internal mechanism created by each particular bundle disposition, and each one reflects differently on the $\bar{\mathbf{C}}$ and $\bar{\bar{\mathbf{C}}}$ matrices. And as a consequence, on the effective mechanical properties as well. This is further evidenced in figs. 15, 16, and 17 by noting the distinguished stress concentration along the fiber bundles for each type of composite.

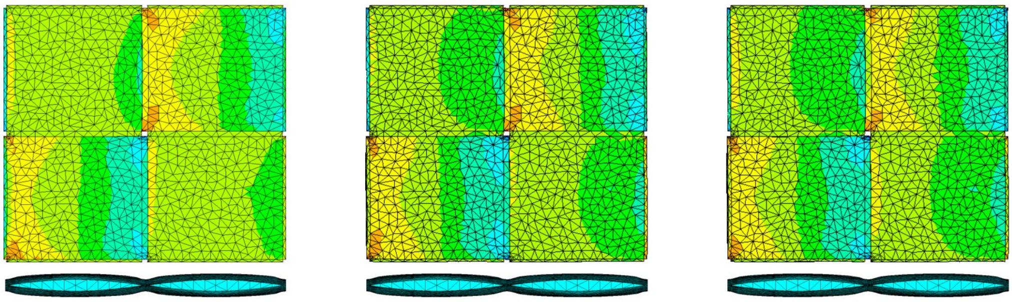

(a) SUBC (b) MBC* (c) PBC

Figure 15: σ_{13} stress/strain response for the plain weave composite under ε^1 strain state, for all boundary conditions studied.

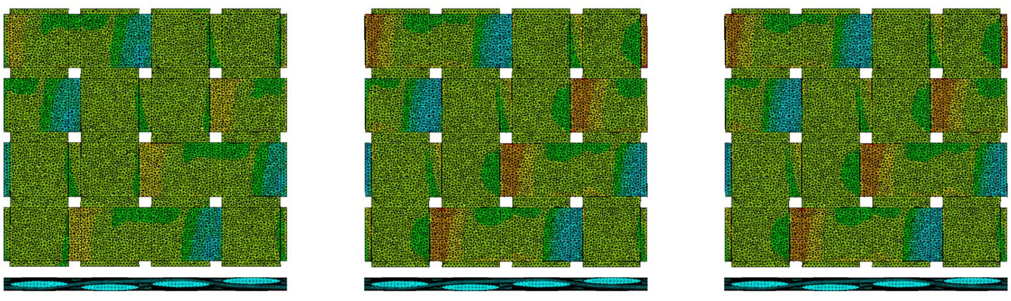

(a) SUBC (b) MBC* (c) PBC

Figure 16: σ_{13} stress/strain response for the 2/2 twill weave composite under ε^1 strain state, for all boundary conditions studied.

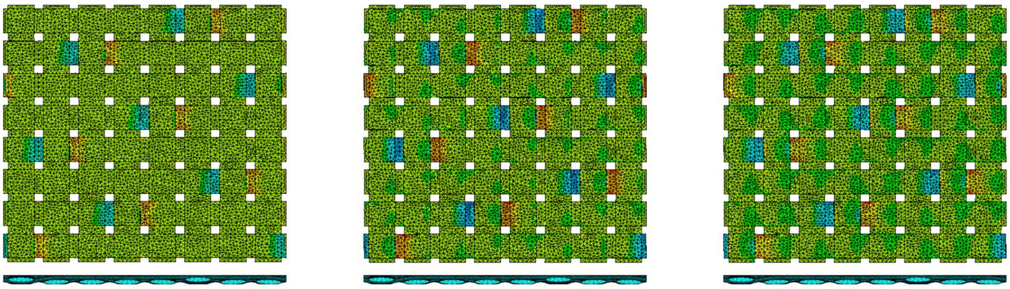

(a) SUBC (b) MBC* (c) PBC

Figure 17: σ_{13} stress/strain response for the plain weave composite under ε^1 strain state, for all boundary conditions studied.

5.4 Overall mechanical response

Aiming at inciting further investigations on the influence of the homogenization and the various boundary conditions on the overall response of a mechanical component, this section presents a simple exercise based on the simulation of a cantilever plate subjected to end moment (Fig. 18). This case emulates a bending-governed problem which can be analyzed using conventional thin plate/shell finite element based on the reduced matrices given in eqs. (91)-(93). The data used for this problem is $L = 300$ mm, $w = 100$ mm, and $h = 1$ mm, with a unit moment at the end, $M = 1$ N mm.

The plots of transverse displacement are shown in figs. 19, 20, and 21 for all three types of textiles studied here. It is evident that the boundary conditions used in the homogenization influence the results, particularly in the case of the 2/2 twill weave. However, the important aspect seems to be the weaving pattern, subject of future investigation, as they could not be compared here due to the difference in material composition, geometry, and fiber fraction of the three textiles studied.

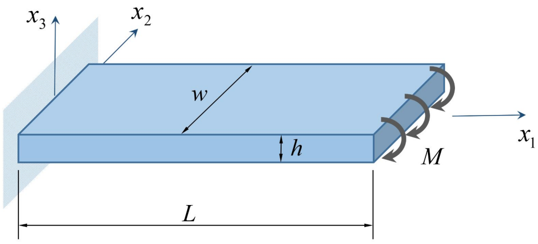

Figure 18: Cantilever plate problem.

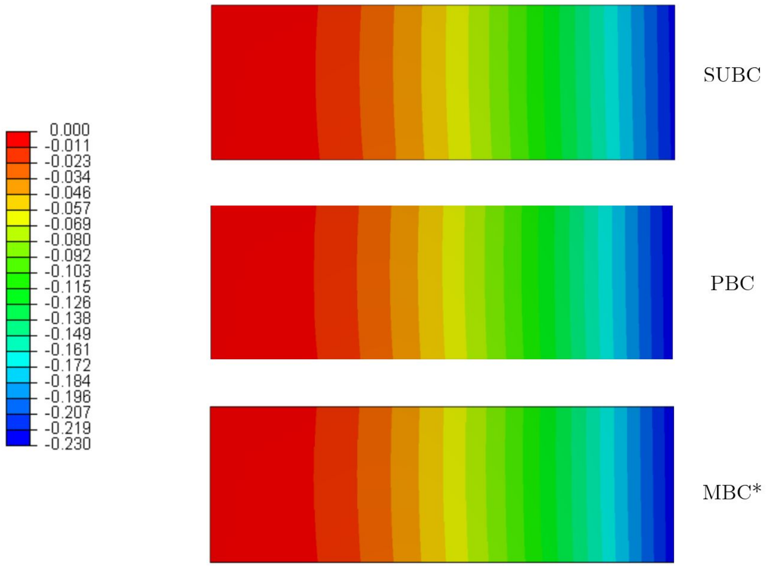

Figure 19: Transverse displacement (u_3) responses of the cantiler plate. Shell finite element results with plain weave properties (91)**.**

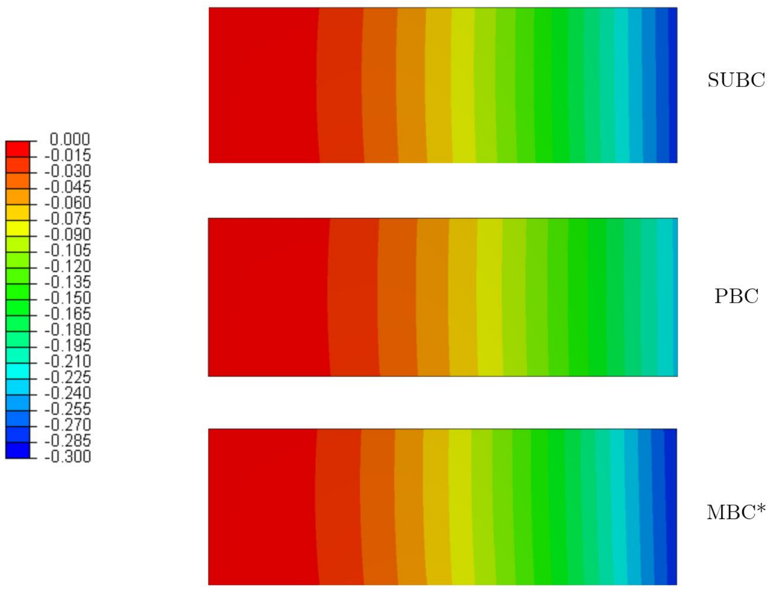

Figure 20: Transverse displacement (u_3) responses of the cantiler plate. Shell finite element results with 2/2 twill weave properties (92)**.**

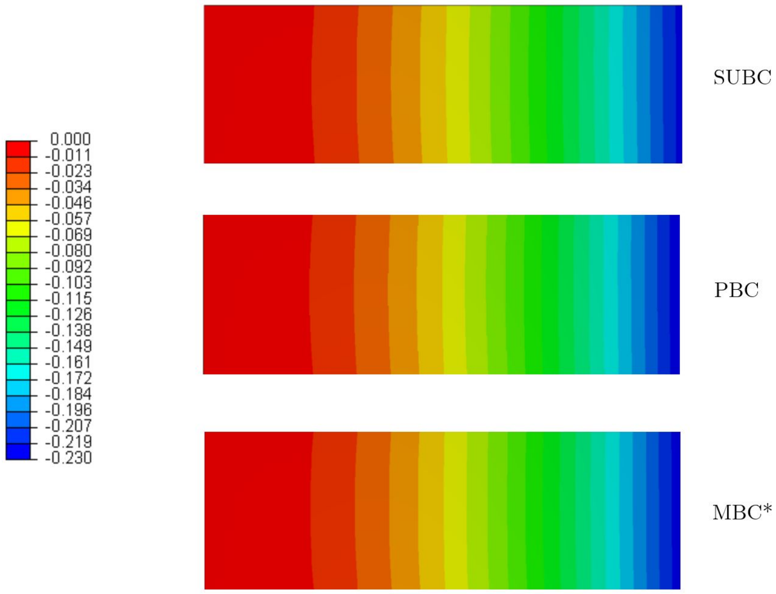

Figure 21: Transverse displacement (u_3) responses of the cantiler plate. Shell finite element results with 8-harness satin weave properties (93)**.**

6 Conclusions

This article discussed some numerical modeling possibilities for the retrieval of the homogenized constitutive matrices of composite textiles whose fiber phase is built through weaving patterns of fiber tows embedded in a linearly elastic matrix phase.

Although the essentials of homogenization via RVE analysis are well understood for simple multi-scale analysis, we showed that the boundary conditions imposed on the RVE may have non-negligible reflexes on the results. In particular, repetitive cells may need other sets of boundary conditions than the uniform displacements commonly employed. We also identify that the usual periodic boundary conditions are not suitable for thin textile composites as plates and shells, as the periodic restrictions along the transverse directions are not the same as the in-plane ones. Aiming at such structures, we proposed a new set of mixed boundary conditions and proved that it complies with the Hill-Mandel criteria.

A second aspect explored in the present study refers specifically to the homogenized constitutive matrices used in the modeling of thin structures. In general, these matrices are computed as suggested by the classical laminate theory, departing from the values of the moduli of the constituents. Because the formulas based on the average field theory cannot take into account the specific weaving pattern of each textile, these formulas are not able to distinguish the variations in stiffness that arise from the different types of interlacing. In such cases, a homogenization approach becomes imperative, altogether with a proper set of boundary conditions. A number of anisotropy indicators were used to compare objectively the variations in the stiffness coefficients for each type of boundary condition. We have shown that the methodology used was able to estimate both 3D and 2D constitutive matrices as well as they are compared to each other and to available results.

References

E. Barbero, J. Trovillion, J. Mayugo, and K. Sikkil. Finite element modeling of plain weave fabrics from photomicrograph measurements. *Composite Structures*, 73(1):41–52, 2006.

E. J. Barbero. *Finite element analysis of composite materials*. CRC press, 2007.

E. de Souza Neto and R. Feijóo. On the equivalence between spatial and material volume averaging of stress in large strain multi-scale solid constitutive models. *Mechanics of Materials*, 40:803–811, 2008.

T. de Vargas Lisbôa and R. J. Marczak. A recursive methodology for the solution of semi-analytical rectangular anisotropic thin plates in linear bending. *Applied Mathematical Modelling*, 48:711–730, 2017.

A. Dixit and H. Mali. Modeling techniques for predicting the mechanical properties of woven-fabric textile composites: a review. *Mech. Compos. Mater.*, 49:1–20, 2013.

J. J. Espadas-Escalante, N. P. van Dijk, and P. Isaksson. A study on the influence of boundary conditions in computational homogenization of periodic structures with application to woven composites. *Composite Structures*, 160:529–537, 2017.

R. Glüge. Generalized boundary conditions on representative volume elements and their use in determining the effective material properties. *Computational materials science*, 79:408–416, 2013.

S. Hazanov and M. Amieur. On overall properties of elastic heterogeneous bodies smaller than the representative volume. *International Journal of Engineering Science*, 33(9): 1289–1301, 1995.

R. Hill. Elastic properties of reinforced solids: some theoretical principles. *Journal of the Mechanics and Physics of Solids*, 11(5):357–372, 1963.

R. Hill. A self-consistent mechanics of composite materials. *Journal of the Mechanics and Physics of Solids*, 13(4):213–222, 1965.

R. Hill. On constitutive macro-variables for heterogeneous solids at finite strain. *Proc R Soc Lond A*, 326:131–147, 1972.

T. Ishikawa. Anti-symmetric elastic properties of composite plates of satin weave cloth. *Fibre Science and Technology*, 15(2):127–145, 1981.

S. Jacques, I. De Baere, and W. Van Paepegem. Application of periodic boundary conditions on multiple part finite element meshes for the meso-scale homogenization of textile fabric composites. *Composites Science and Technology*, 92:41–54, 2014.

R. M. Jones. *Mechanics of composite materials*. CRC press, 2018.

H. Lin, L. P. Brown, and A. C. Long. Modelling and simulating textile structures using texgen. In *Advanced Materials Research*, volume 331, pages 44–47. Trans Tech Publ, 2011.

A. Long and L. Brown. Modelling the geometry of textile reinforcements for composites: Texgen. In *Composite reinforcements for optimum performance*, pages 239–264. Elsevier, 2011.

R. Luciano and E. Sacco. Variational methods for the homogenization of periodic heterogeneous media. *European Journal of Mechanics-A/Solids*, 17(4):599–617, 1998.

J. Mandel. *Plasticité Classique et Viscoplasticité*. CISM Lecture Notes No. 97. Springer, 1998.

K. Mazumda, S. *Composites manufacturing: materials, product, and process engineering*. CRC Press, 2002.

Z. ming Huang. The mechanical properties of composites reinforced with woven and braided fabrics. *Composites science and technology*, 60(4):479–498, 2000.

S. Nemat-Nasser and M. Hori. Micromechanics: overall properties of heterogeneous materials, 1996.

A. T. Nettles. NASA-RP-1351 - basic mechanics of laminated composite plates". Nasa ref. publ. 135, NASA Marshall Space Flight Center, 1994.

O. Rand and V. Rovenski. *Analytical methods in anisotropic elasticity: with symbolic computational tools*. Springer Science & Business Media, 2007.

S. I. Ranganathan and M. Ostoja-Starzewski. Universal elastic anisotropy index. *Physical review letters*, 101(5):055504, 2008.

M. V. Rao, P. Mahajan, and R. Mittal. Effect of architecture on mechanical properties of carbon/carbon composites. *Composite Structures*, 83(2):131–142, 2008.

J. N. Reddy. *Mechanics of laminated composite plates and shells: theory and analysis*. CRC press, 2003.

B. V. Sankar and R. V. Marrey. Analytical method for micromechanics of textile composites. *Composites Science and Technology*, 57(6):703–713, 1997.

D. Scida, Z. Aboura, M. Benzeggagh, and E. Bocherens. Prediction of the elastic behaviour of hybrid and non-hybrid woven composites. *Composites science and technology*, 57(12):1727–1740, 1998.

D. Scida, Z. Aboura, M. Benzeggagh, and E. Bocherens. A micromechanics model for 3d elasticity and failure of woven-fibre composite materials. *Composites Science and Technology*, 59(4):505–517, 1999.

H. Shen and L. C. Brinson. A numerical investigation of the effect of boundary conditions and representative volume element size for porous titanium. *Journal of Mechanics of Materials and Structures*, 1(7):1179–1204, 2006.

Z. Ullah, X.-Y. Zhou, L. Kaczmarczyk, E. Archer, A. McIlhagger, and E. Harkin-Jones. A unified framework for the multi-scale computational homogenisation of 3d-textile composites. *Composites Part B: Engineering*, 167:582–598, 2019.

T. Zohdi. Computational modeling and design of new random microheterogeneous materials. *CISM Course Notes*, 1, 2002.